CAMBRIDGE JOURNALS

Proof Delivery Form

Geological Magazine

Date of delivery:

Journal and vol/article ref: geo 2100116

Number of pages (not including this page): 28

This proof is sent to you on behalf of Cambridge University Press. Please check the proofs carefully. Make any corrections necessary using the Comments button to add or delete text and answer queries on each page of the proofs

Please return the **marked proof** within 2 days of receipt to:

geoproduction@cambridge.org

Authors are strongly advised to read these proofs thoroughly because any errors missed may appear in the final published paper. This will be your ONLY chance to correct your proof. Once published, either online or in print, no further changes can be made.

To avoid delay from overseas, please send the proof by airmail or courier.

If you have **no corrections** to make, please email **geoproduction@cambridge.org** to save having to return your paper proof. If corrections are light, you can also send them by email, quoting both page and line number.

- The proof is sent to you for correction of typographical errors only. Revision of the substance of the text is not permitted, unless discussed with the editor of the journal. Only **one** set of corrections are permitted.
- Please answer carefully any author queries.
- Corrections which do NOT follow journal style will not be accepted.
- A new copy of a figure must be provided if correction of anything other than a typographical error introduced by the typesetter is required.

- If you have problems with the file please contact **geoproduction@cambridge.org**

Please note that this pdf is for proof checking purposes only. It should not be distributed to third parties and may not represent the final published version.

Important: you must return any forms included with your proof. We cannot publish your article if you have not returned your signed copyright form.

NOTE - for further information about **Journals Production** please consult our **FAQs** at http://journals.cambridge.org/production_faqs

QUERIES

AQ1: The distinction between surnames can be ambiguous, therefore to ensure accurate tagging for indexing purposes online (e.g. for PubMed entries), please check that the highlighted surnames have been correctly identified, that all names are in the correct order and spelt correctly.
AQ2: Please check that affiliations of all the authors and the corresponding author details are correctly set.
AQ3: Please provide missing city and country in affiliation details.
AQ4: Kaver changed to Km. Please check this is correct
AQ5: Length of hammer for scale is XX cm. Please add the length of the hammer.
AQ6: 8-la changed to 8e. Please check this is correct.
AQ7: Diameter of coin for scale is XX cm. Please add the diameter of the coin.
AQ8: Length of hammer for scale is XX cm. Please add the length of the hammer.
AQ9: Width of hammer head for scale is XX cm. Please add the width of the hammer head.
AQ10: Length of pencil for scale is XX cm. Please add the length of the pencil.
AQ11: Length of hand lens for scale is XX cm. Please add the length of the hand lens.
AQ12: Length of hammer for scale is XX cm. Please add the length of the hammer.
AQ13: Fig. S1d changed to S1e. Please check this is correct.
AQ14: Fig. S1d changed to S1e. Please check this is correct.
AQ15: Hr – remanent coercive force. Please can you check this is correctly defined.
AQ16: 50.3 ± 5.8. Should this be ± 5.9 as in the text?
AQ17: * Kinetic parameters. Please can you indicate what should be labelled as kinetic parameters in the table.
AQ18: Fig. 18e changed to 18d. Please check this is correct.
AQ19: Al_2O_3 versus MgO changed to MgO versus FeO_T. Please check this is correct.
AQ20: equation 5 changed to equation 2. Please check this is correct
AQ21: Fig. S1e changed to S1f. Please check this is correct.
AQ22: Final degree project in geology, Universidad Nacional de Río Negro, Argentina. Published thesis. Please check this is correct.
AQ23: “Baxter and Feely (2002” has not been cited in the text. Please indicate where it should be cited or delete it from the Reference List.
AQ24: “Hrouda (1982)” has not been cited in the text. Please indicate where it should be cited or delete it from the Reference List.
AQ25: “Ridolfi et al. (2008)” has not been cited in the text. Please indicate where it should be cited or delete it from the Reference List.
AQ26: “Rovere et al. (2004)” has not been cited in the text. Please indicate where it should be cited or delete it from the Reference List.
AQ27: “Yavuz (2003)” has not been cited in the text. Please indicate where it should be cited or delete it from the Reference List.

Geological Magazine

www.cambridge.org/geo

Original Article

Cite this article: Assis OS, Zaffarana CB, Orts D, Puigdomenech C, Ruiz González V, Gallastegui G, Hauser N, Kiseeva ES, Molina JF, and Pernich S. Emplacement conditions and exhumation of the Varvarco Tonalite and associated plutons from the Cordillera del Viento, Southern Central Andes. *Geological Magazine* https://doi.org/10.1017/S0016756821001163

Received: 24 March 2021
Revised: 6 October 2021
Accepted: 18 October 2021

Keywords:
granitoids; Andean orogeny; AMS; fission-track dating; fast exhumation rate

Author for correspondence:
Omar Sebastian Assis,
Email: seba_assis@outlook.com; sebaoassis@gmail.com

Emplacement conditions and exhumation of the Varvarco Tonalite and associated plutons from the Cordillera del Viento, Southern Central Andes

Omar Sebastian Assis[1], Claudia Beatriz Zaffarana[2], Darío Orts[2], Carla Puigdomenech[3], Víctor Ruiz González[3], Gloria Gallastegui[4], Natalia Hauser[1], Ekaterina S. Kiseeva[5], José Francisco Molina[6] and Sebastián Pernich[2]

[1]Instituto de Geociências, Universidade de Brasília, Laboratório de Geocronologia e geoquímica isotópica, Brasília, 70910 900, DF, Brasil; [2]Universidad Nacional de Río Negro, Sede Alto Valle-Valle Medio, General Roca e Instituto de Investigación en Paleobiología y Geología (IIPG-CONICET); [3]Instituto de Geociências Básicas, Aplicadas y Ambientales de Buenos Aires (IGeBA); CONICET; Universidad de Buenos Aires; [4]Instituto Geológico y Minero de España (IGME, CSIC), España; [5]School of Biological, Earth and Environmental Sciences, University College Cork, Distillery Fields, North Mall, Cork, Ireland and [6]Departamento de Mineralogía y Petrología, Universidad de Granada, España

Abstract

During the Late Cretaceous Andean orogeny, the compressive deformation associated with the shallowing of the subducting slab caused the development of the arc-related igneous rocks known as the Naunauco Belt. This study presents petrographic, mineralogical and anisotropy of magnetic susceptibility data for the Varvarco Intrusives (the Varvarco Tonalite, Butalón Tonalite and Radales Aplite), which crop out in the Cordillera del Viento, Neuquén Province, Argentina. The assembly of plutons was formed by mafic magma episodic injection. Amphibole and biotite compositions suggest that the Varvarco Tonalite is related to calc-alkaline, I-type magmas, typical of subduction environments. Different geothermobarometers based on amphibole and plagioclase compositions for the Varvarco Tonalite suggest shallow emplacement conditions (~2–3 kbar, equivalent to ~12 km depth). Apatite fission-track analyses give exhumation ages of 67.5 ± 8 Ma for the Varvarco Tonalite and 50.3 ± 5.9 Ma for the Butalón Tonalite. A calculated continuous fast exhumation rate of at least 330 °C Ma^{-1} is consistent with the shallow emplacement conditions, textural data and geobarometric estimations. In agreement with the thermal profile, the magmatic system was exhumed by ~12 km within *c.* 2.1 Ma implying a geothermal gradient of ~62.5 °C km^{-1}. The last step of exhumation occurred between ~65.3 and 56.9 Ma. The magmatic fabrics observed in the studied plutons reflect mostly magma chamber processes. The Varvarco Intrusives represent satellite calc-alkaline plutons of the North Patagonian Batholith which were emplaced syn- to post-tectonically with respect to a major deformation stage of the Southern Central Andes.

1. Introduction

Cordilleran batholiths are large magmatic bodies that result from the accumulation of many smaller plutons, spatially and chemically associated, which may or may not be temporally related. Most of these batholiths are composed of granodiorite and tonalite, such as the Sierra Nevada Batholith (Bateman & Eaton, 1967) and the North Patagonian Batholith (Ramos *et al.* 1982). The Patagonian Batholith represents a large granite intrusive complex that extends from 39° to 56° S, and is mainly composed of tonalites (Ramos *et al.* 1982). The main peak of intrusion relates to the development of the North Patagonian Batholith formed in Early Cretaceous time, between 136 and 127 Ma (Pankhurst *et al.* 1999; Hervé *et al.* 2007), slightly before the onset of Late Cretaceous compression coeval with the Neuquén foreland basin development (Ramos, 1999). In addition, in Late Cretaceous–Palaeogene times, the magmatic arc was expanded into the retro-arc region, including the present-day Cordillera del Viento range, by the intrusion of satellite igneous bodies at 130–150 km east of the present arc trend (Hervé *et al.* 2007; Fig. 1).

Here, we study the internal structure of some of these satellite igneous bodies, the Varvarco Intrusives (Varvarco Tonalite, Radales Aplite and Butalón Tonalite) that are exposed in the Varvarco–Butalón region in the Cordillera del Viento (Neuquén Andes; Figs 1, 2a). We applied the anisotropy of magnetic susceptibility (AMS) method, combined with petrographic and mineral chemistry data to define magmatic structures and, thus, to infer magma emplacement

CAMBRIDGE UNIVERSITY PRESS

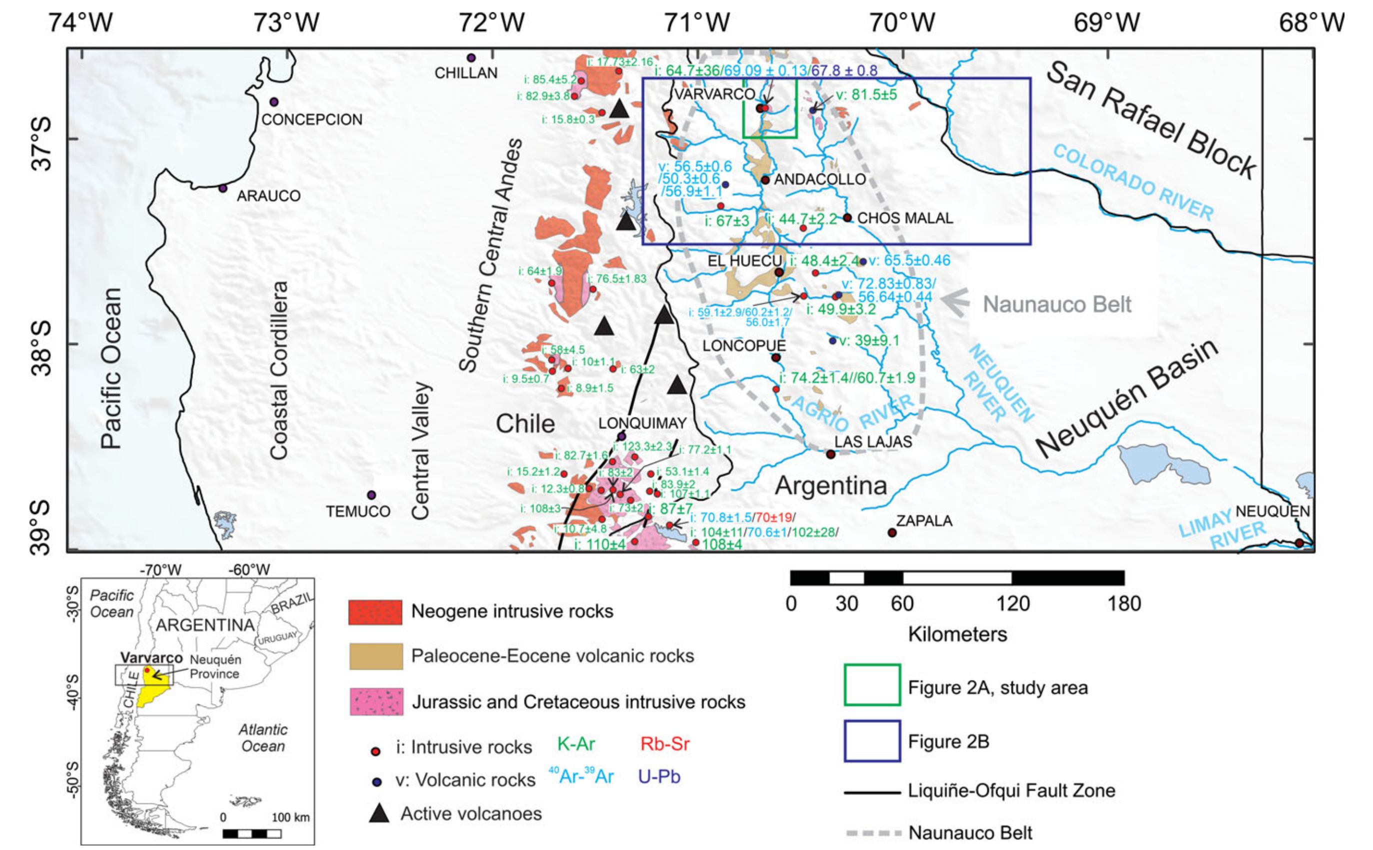

Fig. 1. (Colour online) Regional geological map of the Southern Central Andes. Ages for intrusive and volcanic rocks are listed in online Supplementary Material Table S1. Black rectangle indicates study area (Fig. 2a, b). The Naunauco Belt is marked with a grey dotted line; it comprises both plutonic rocks of Late Cretaceous–Palaeogene age and volcanic rocks of Paleocene–Eocene age. Numbers indicate ages obtained by different methods, as shown in legend.

mechanisms. The AMS method has been proven to be a very useful tool to study the internal structure of weakly foliated bodies (e.g. Archanjo *et al.* 1995, 2002; de Saint Blanquat & Tikoff, 1997; Ferré & Améglio, 2000; McNulty *et al.* 2000; Neves *et al.* 2003; Žák *et al.* 2005; D'Eramo *et al.* 2006; Stevenson, 2009; Somoza *et al.* 2015; Nédélec & Bouchez, 2015; Olivier *et al.* 2016; Zaffarana *et al.* 2017). In particular, the AMS method is relevant for the resolution of magmatic lineations, which are generally hard to measure in the field. The interpretation of the internal structure of plutons and their relationship with the country rock may be classified into three main types: reflecting the internal magma chamber, regional deformation processes (Paterson *et al.* 1998), or a combination of both.

The timing of intrusion with respect to the exhumation of the Varvarco Tonalite and the Butalón Tonalite was also investigated by obtaining apatite fission-track ages for these intrusives. Crustal thickness estimates at the time of magma generation were aided by geochemical data (mineral chemistry for amphibole, plagioclase and biotite), with the aim of developing a model for emplacement and exhumation of the Varvarco Tonalite. Mineral compositions were used to constrain the magma chamber temperature and depth through geothermobarometric analysis (Hammarstrom & Zen, 1986; Hollister *et al.* 1987; Johnson & Rutherford, 1989; Schmidt, 1992; Holland & Blundy, 1994; Anderson & Smith, 1995; Ridolfi *et al.* 2010; Ridolfi & Renzulli, 2012; Putirka, 2016; Molina *et al.* 2015, 2021). The combination of these methods allows us to unravel the history of the Varvarco satellite intrusives, from their emplacement to fast exhumation during the Late Cretaceous–Palaeogene period of the Andean orogeny.

2. Geological and structural framework

The three plutons investigated in this work, the Varvarco Tonalite, the Butalón Tonalite and the Radales Aplite, are located in the Varvarco and Butalón areas (Fig. 2a) and were originally named by Pesce (1981) as the Varvarco Intrusives. They were later attributed to the Colipilli Formation (Franchini *et al.* 2003; Kay *et al.* 2006; Casé *et al.* 2008), the intrusive part of the volcanic and plutonic Late Cretaceous Naunauco Belt (Llambías & Malvicini, 1978; Zamora Valcarce *et al.* 2011).

Pesce (1981) had originally described the Varvarco pluton as a granodiorite body, but the average modal composition that we found in all our sites is more compatible with a tonalitic intrusive. Therefore, we renamed this pluton the Varvarco Tonalite. In the same way, the Radales Granite (Zanettini *et al.* 2001) is renamed here the Radales Aplite because its general texture is aplitic, typical of subvolcanic igneous bodies.

The Varvarco Tonalite has a K–Ar cooling age (whole-rock) of 64.7 ± 3.2 Ma (J.I.C.A./M.M.A.J., 2000 *in* Franchini *et al.* 2003) and an ^{40}Ar–^{39}Ar cooling age for biotite of 69.09 ± 0.13 Ma (Kay *et al.* 2006). A U–Pb SHRIMP zircon age of 67.8 ± 0.8 Ma was thoroughly documented by Assis (2019); thus, the crystallization age of the Varvarco Tonalite coincides with the K–Ar cooling age. The geochemistry of the Butalón Tonalite was studied by Casé

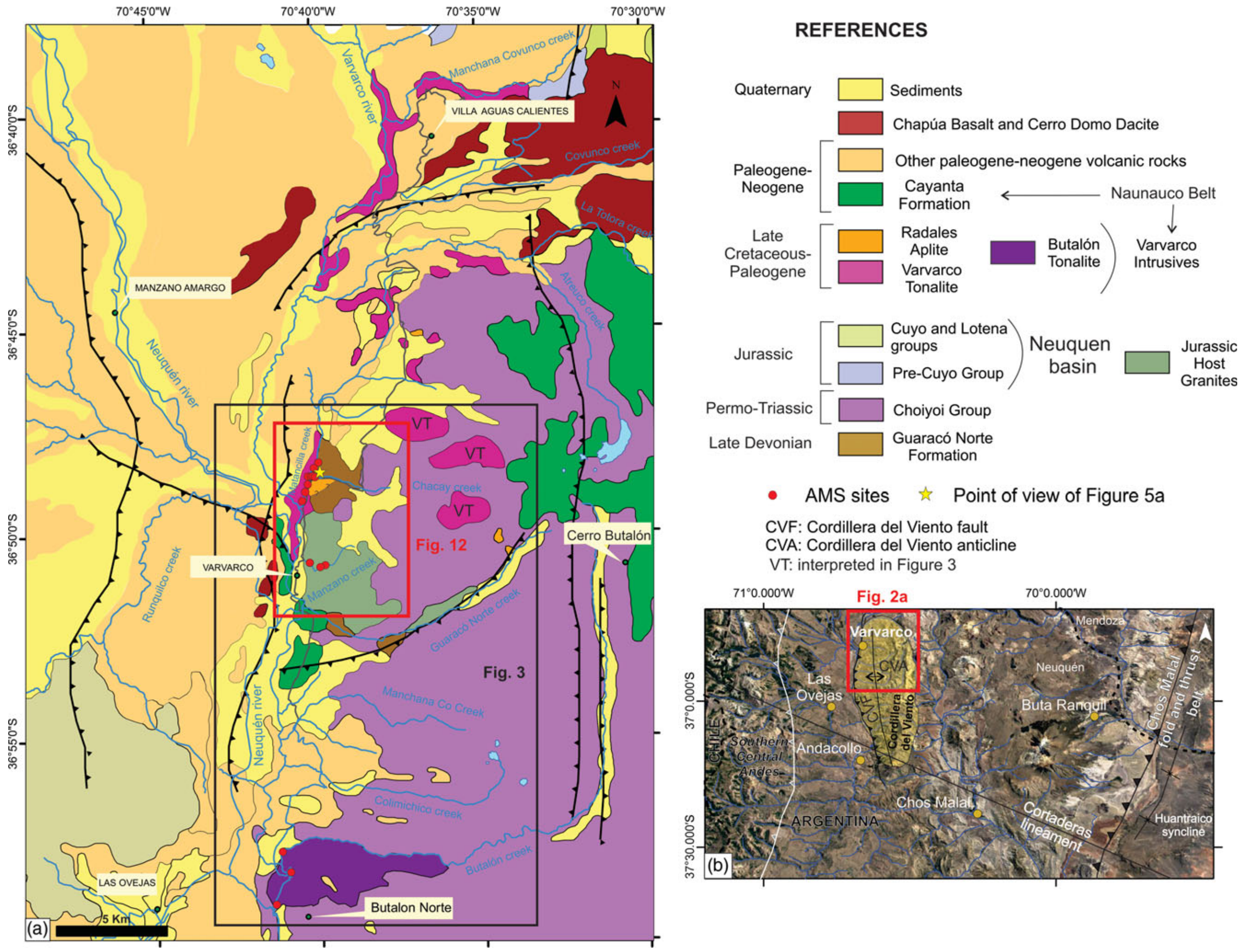

Fig. 2. (Colour online) (a) Local and (b) regional maps of the study area. The maps are based on Zanettini *et al.* (2001), Ramos *et al.* (2011), Giacosa *et al.* (2014) and Sagripanti *et al.* (2014). Black rectangle indicates the area in Figure 3, and red rectangle indicates the area of Figure 12.

et al. (2008), who indicated that these igneous rocks are meta- to peraluminous calc-alkaline with low to medium K_2O contents, coincidental with I-type granitoids like other granitoids in the area (e.g. Cerro Nevazón; Franchini *et al.* 2003). The Radales Aplite is a granophyric granite intruding the Varvarco Tonalite (Zanettini *et al.* 2001). The Au–Ag veins that intrude the Radales Aplite and Permian and Jurassic rocks were dated by the ^{40}Ar–^{39}Ar step-wise method in adularia and yielded an age of 65.68 ± 0.22 Ma (Zappettini *et al.* 2014). These ^{40}Ar–^{39}Ar data indicate that the break between the emplacement of the Varvarco Tonalite and the intrusion of the Radales Aplite was short.

The Varvarco Intrusives crop out in the Cordillera del Viento range in the Neuquén Andes of southwestern Argentina, which is a structurally complex area, with convergence of structures developed during different periods of time. The currently observed structural features in this region were mainly formed between Late Cretaceous and Miocene times (Giacosa *et al.* 2014; Turienzo *et al.* 2018; Sánchez *et al.* 2018), when the main compressive structures were developed (Fig. 2a, b).

The Cordillera del Viento Fault is one of the main compressional structures formed by the inversion of N–S normal faults that controlled the Late Triassic to Early Jurassic rift sedimentation in the westernmost part of the Neuquén Basin (Vergani *et al.* 1995). During the Andean orogeny, in pre-Eocene times, the inversion of the extensional system occurred, and the Cordillera del Viento Fault became a reverse fault that uplifted Palaeozoic rocks to form the Cordillera del Viento Anticline (Giacosa *et al.* 2014).

The core of the Cordillera del Viento Anticline (Giacosa *et al.* 2014) exposes a basement of middle Palaeozoic metamorphic rocks (Fig. 2a), grouped together in the Guaracó Norte Formation (Zappettini *et al.* 1987; Zanettini *et al.* 2001). These rocks include quartz-rich metasandstones and laminated quartzite layers, with slates towards the top of the sequence which are all cut by numerous quartz and granitic veins (Giacosa *et al.* 2014). The sedimentary protolith is characterized by rhythmic alternation of sandstone and pelite layers showing current ripples (Giacosa *et al.* 2014). The age of the Guaracó Norte Formation is Late Devonian, considering a maximum depositional age, based on the youngest peak of 369 ± 5 Ma (younger than 374 Ma and older than 326 Ma, U–Pb SHRIMP dating of detrital zircon; Zappettini *et al.* 2012).

The Carboniferous sedimentary rocks of the Cordillera del Viento crop out south of the study area, near the Andacollo locality (Fig. 2b), and they are grouped into the Andacollo Group (Digregorio, 1972; Digregorio & Uliana, 1980; Llambías *et al.* 2007). Volcanic and plutonic facies from the Permo-Triassic Choiyoi Group (Stipanicic, 1966; Digregorio, 1972) crop out in the Cordillera del Viento. In the Varvarco area, the Choiyoi

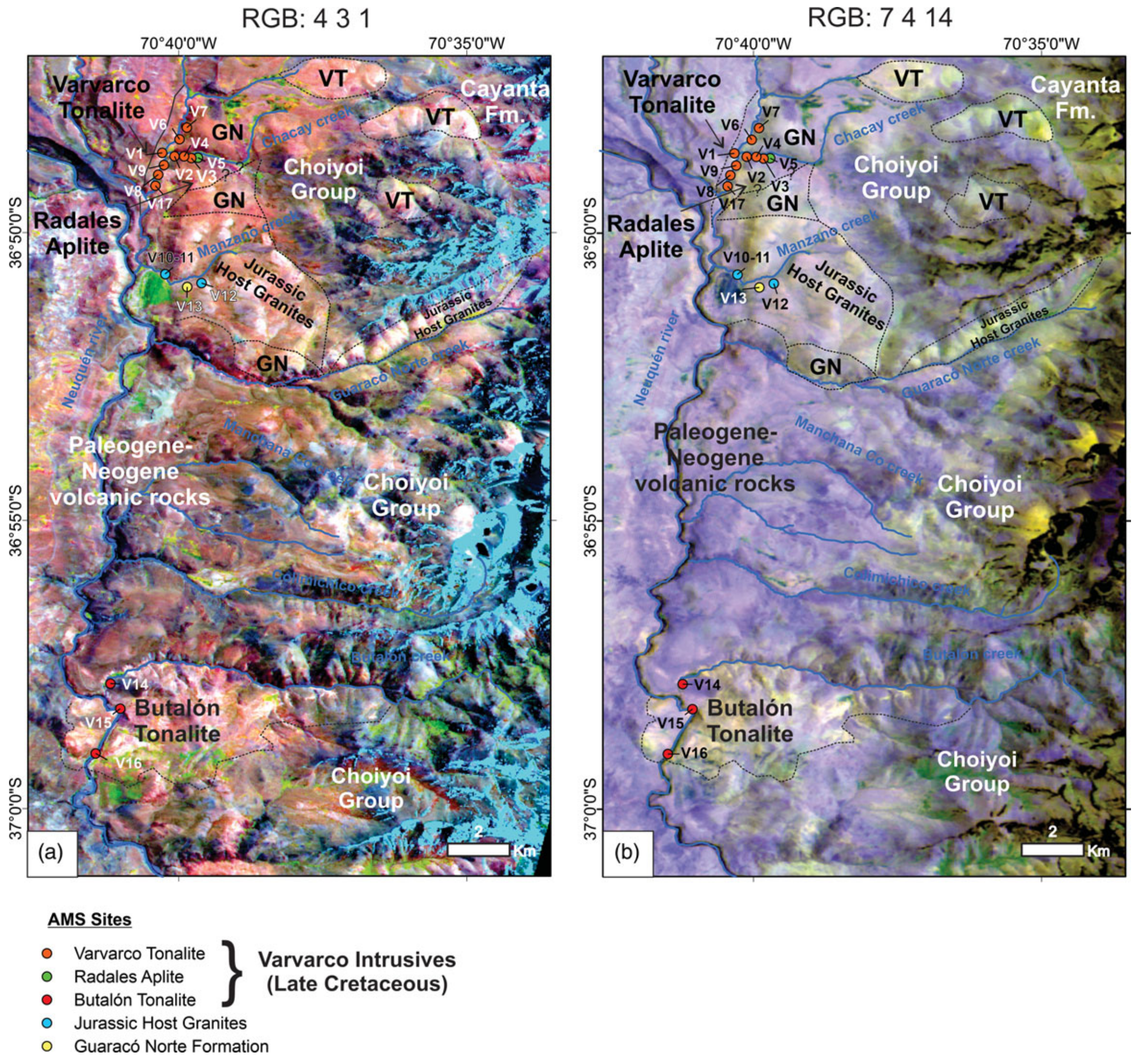

Fig. 3. (Colour online) ASTER images of the study area: (a) RGB: 4 6 1 and (b) RGB: 7 4 14. VT – Varvarco Tonalite; GN – Guaracó Norte Formation.

Group is composed of two sections, where andesites and rhyolites predominate in the lower and upper sections, respectively (Digregorio, 1972; Zanettini *et al.* 2001).

An extensional deformation period, associated with Gondwana break-up, is registered for the Cordillera del Viento. This extensional phase initiated N–S-trending and NNE–SSW-trending faults in the northern part of the Cordillera del Viento to E–W-trending faults in the southern part, where interbedded shale strata and ignimbrites with wedge geometry are separated by normal faults (Giacosa *et al.* 2014). Magnetic and gravimetric data, combined with field observations, suggest that Late Triassic rifting in the Cordillera del Viento area would have taken place in a regional WNW–ESE to NW trend, with minor local NE-trending structures (Sagripanti *et al.* 2014). Magnetic data revealed that basement rocks are segmented by nearly orthogonal structures (Sagripanti *et al.* 2014).

Between the Late Triassic and Cenozoic periods, the Neuquén Basin (Fig. 1) developed between 32° and 40° S (e.g. Howell *et al.* 2005). During Jurassic and Early Cretaceous times, the Palaeo-Pacific Ocean transgressions produced marine strata that alternated with the deposition of continental sequences in the back-arc setting of this basin, which was affected by thermal subsidence (Legarreta & Uliana, 1991; Vergani *et al.* 1995; Howell *et al.* 2005; Arregui *et al.* 2011).

On the eastern flank of the Cordillera del Viento, the Lower to Upper Jurassic syn-rift deposits of the early phase of the Neuquén Basin crop out, characterized by variable thicknesses and normal fault associations (Sagripanti *et al.* 2014). The Pre-Cuyo Group (Hettangian–Sinemurian) is represented by the Cordillera del Viento and Milla Michicó formations (Gulisano *et al.* 1984; Riccardi & Stipanicic, 2002). The Jurassic Cuyo and Lotena groups crop out in the northeastern corner of the studied area (Suárez & de la Cruz, 1997; Leanza *et al.* 2005; Llambías *et al.* 2007; Fig. 2).

We discovered that an igneous body, previously assigned to the Radales Aplite, has an Early Jurassic age (185 ± 3 Ma). This aplite is here referred to by the informal designation Jurassic Host Granites (Figs 2a, 3a, b). These felsic intrusives are coeval with the Pre-Cuyo Group. The provisional name highlights that they are a part of the host rocks for the Late Cretaceous granites studied in this work.

As mentioned in Section 1, the Andean orogeny was mainly active in the Cordillera del Viento region between Late Cretaceous and Miocene times. The Andean orogeny reactivated Late Triassic WNW–ESE to NW and NE-trending normal structures (Giacosa *et al.* 2014; Turienzo *et al.* 2018; Sánchez *et al.* 2018).

Sánchez *et al.* (2018) reported zircon (U–Th)/He thermochronological ages of from 72.2 ± 2.8 Ma to 66.0 ± 6.1 Ma, and the apatite fission-track ages are 51.7 ± 3.2 Ma and 56.5 ± 10.7 Ma for exhumation in the Chos Malal fold-and-thrust belt. The WNW–ESE- and NW-trending structures acted as transfer zones, whereas the NE-trending ones acted as frontal contractional structures (Sagripanti *et al.* 2014). The N–S-trending structures have been interpreted as the result of Andean deformation, as these contractional structures are not related to the rifting architecture and cross-cut the depocentres (Sagripanti *et al.* 2014; Giacosa *et al.* 2014). The studies concluded that Andean crustal shortening caused the formation of the N–S-trending faults and thrusts, and associated folds, as well as W–E- to WNW–ESE-trending strike-slip structures. The latter are regarded as lateral structures that control the N and S propagation of the Andean thrusts.

During the Andean compressive stage in middle Cretaceous time and slightly after, volcanic rocks of the Cayanta Formation (Rapela & Llambías, 1985) were extruded, and subvolcanic magmatic bodies were emplaced into a satellite position with respect to the present magmatic arc in Late Cretaceous–Palaeogene times (Llambías & Rapela, 1989; Franchini *et al.* 2003; Cobbold & Rossello, 2003; Hervé *et al.* 2007; Zamora Valcarce, 2007; Llambías & Aragón, 2011; Spagnuolo *et al.* 2012; Figs 1, 2a).

3. Analytical methods

Field studies were carried out in the area of the Varvarco, Radales and Butalón plutons, and their host rocks, resulting in 23 thin-sections for petrographic studies. The AMS study was performed on 17 sites, of which nine sites belong to the Varvarco Tonalite, three sites to the Butalón Tonalite, one site to the Radales Aplite, three sites to the Jurassic Host Granites and one site to the Guaracó Norte Formation. A portable rock drill for palaeomagnetic sampling was used. From each site we collected at least five orientated cylinders, summing up to a total of 95 specimens (Table 1). The cylinders were orientated using solar and magnetic compasses. Sites are presented in Table 1; their distribution is located along roads and creeks (Fig. 2a).

The high elevation of the Cordillera del Viento region makes it difficult to map the exact morphology of the Varvarco, Radales and Butalón igneous bodies. ASTER level 1B data were used to complement the mapping of the plutonic bodies (Fig. 3a, b). The studied geological units at 1:200 000 scale are presented in Figures 2a and 3a, b. Their recognition in ASTER satellite images was possible through combining two false-colour RGB compositions (RGB: 4 3 1 and RGB: 7 4 14), as shown in Figures 3a and b, respectively. False-colour RGB composition 7 4 14 is useful to discriminate rocks with different silica contents. In the map shown in Figure 3b the orange/yellow regions correspond to felsic litho-units that are richer in quartz, as shown by the diagnostic SiO-bond spectral absorption at 10.30–11.70 µm (Clark, 1999; bands 13–14 in ASTER).

3.a. Anisotropy of magnetic susceptibility (AMS)

An MFK1-B Kappabridge susceptibilimeter, located at the IGEBA, CONICET, Argentina, was used to perform the AMS measurements. A minimum of five specimens per site were used (Jelínek, 1978, 1981) to obtain the AMS ellipsoids (with principal axes K1 > K2 > K3) with the programs ANISOFT 4.2 (Chadima & Jelinek, 2009).

The rock magnetic fabric is defined by the three principal axes of the AMS ellipsoid (K1 > K2 > K3; Bouchez, 2000). A magnetic lineation is defined parallel to K1. A magnetic foliation is the plane containing K1 and K2, with K3 being the pole to foliation. The magnetic lineation is parallel to the structural lineation (stretching or flow), and the magnetic foliation is parallel to the structural foliation (flattening or flow; Borradaile & Henry, 1997). However, sometimes this relationship may be obliterated by fabric overprinting or by the presence of single-domain magnetite (e.g. Rochette *et al.* 1992, 1999; Borradaile & Henry, 1997).

The domain state of magnetite was studied using the diagram of Day *et al.* (1977), which was constructed with the Hc, Ms and Mr (coercive force, saturation magnetization and remanent magnetization, respectively) hysteresis parameters, together with the remanent coercive force Hcr (obtained from the backfield curve; Bouchez, 2000). Anhysteretic remanence measurements (Somoza *et al.* 2015) were also performed in some representative samples to check the coaxial behaviour of the ferromagnetic and paramagnetic fabric of the rocks.

The minerals that control the magnetic fabric were investigated by hysteresis curves, isothermal remanent magnetization and backfield analyses in six representative samples (four from the Varvarco Tonalite and two from the Jurassic Host Granites). The anisotropy of anhysteretic remanent magnetization (AARM; e.g. Somoza *et al.* 2015) was applied in three sites. Measurements were performed in the Department of Earth and Environment Sciences, Ludwig-Maximilians University in Munich, using equipment called a 'SushiBar' (Wack & Gilder, 2012).

3.b. Apatite fission-track dating (AFT)

Apatite fission tracks (AFT) from samples VAR5 from the Varvarco Tonalite and BU4 from the Butalón Tonalite were analysed in the LA.TE. ANDES laboratory (https://www.lateandes.com), Salta, Argentina. Both apatite fractions were obtained by mechanical separation, magnetic separation (Frantz isodynamic separator) and heavy liquid treatment (LTS and diiodomethane). Approximately 100 apatite crystals for each sample were then mounted in epoxy. In general, the apatite crystals are subhedral to euhedral, and fractured. The mounted samples were polished and then leached under nitric acid (HNO_3) 5.5 N for 20 seconds at 20 °C to reveal spontaneous tracks. The samples were then irradiated with the External Detector in the RA-3 Reactor (Centro Atómico Ezeiza, Buenos Aires, Argentina). The irradiation process took place over 76 hours, with a fluency of 7×10^{15} n cm^{-2}. After the decay period in the reactor, the batch was sent back to the LA.TE. ANDES S.A. laboratory for the fission-track measurements. Overall, ~35 grains were used for measurements with a surface greater than 600 µm^2. Areas with obvious crystallographic dislocations were avoided.

All measurements were made with a Zeiss AXIO Imager Z2m binocular microscope. The system is equipped with the TrackWorks Autoscan software, which carried out the counting of the tracks and determination of other parameters, such as fission-track etch pit diameter (Dpar). The ages were determined with the ζ value method from Hurford & Green (1982, 1983) and Wagner *et al.* (1992). Data processing was done using Trackkey software (Dunkl, 2002) that allowed age calculation. The uncertainty on obtained ages is reported at the 1–2 σ level (Fig. 15a, b).

3.c. Electron microprobe analysis

Electron microprobe analysis of major-element concentrations was performed at the Technical-Scientific Services of Oviedo University (Spain) using a Cameca SX-100 electron microprobe

AQ4

Table 1. AMS sites of the Varvarco, Radales and Butalón plutons, Jurassic Host Granites and Guaracó Norte Formation

Site	Lithology	GPS data	N	Km	K1d	K1i	C1a	C1b	K2d	K2i	C2a	C2b	K3d	K3i	C3a	C3b	K1	K2	K3	Lmean	Fmean	Pmean	Pjmean	Tmean
V1	Varvarco Tonalite (main facies)	36° 48′ 36.1″ S; 70° 40′ 14.6″ W	5	5.98E-02	143.2	74.5	8.3	3.5	337.7	15.1	9.9	2.9	246.7	3.7	6.6	4.1	1.087	0.982	0.931	1.107	1.055	1.167	1.170	−0.312
V2		36° 48′ 36.3″ S; 70° 40′ 09.5″ W	5	1.86E-02	137.2	47.8	23.9	19.5	5.2	31.2	32.4	20.5	258.6	25.3	32.7	15.9	1.023	0.997	0.980	1.026	1.017	1.044	1.044	−0.189
V3		36° 48′ 36.4″ S; 70° 40′ 04.3″ W	7	1.15E-02	323.2	3.5	20.8	9.9	53.8	8.6	21.0	8.5	211.2	80.7	10.9	7.9	1.019	0.999	0.982	1.019	1.018	1.037	1.037	−0.051
V6		36° 48′ 23.8″ S; 70° 40′ 03.2″ W	6	4.70E-02	68.7	59.2	18.6	6.7	338.0	0.4	33.5	8.4	247.7	30.8	31.9	6.2	1.050	0.986	0.963	1.065	1.024	1.091	1.094	−0.457
V7		36° 48′ 15.7″ S; 70° 39′ 55.0″ W	6	1.23E-02	63.7	61.2	11.0	4.9	306.1	14.3	49.5	10.4	209.4	24.4	49.5	5.1	1.069	0.980	0.951	1.090	1.031	1.124	1.129	−0.478
V8		36° 48′ 58.7″ S; 70° 40′ 20.2″ W	5	4.20E-02	124.9	53.5	21.6	10.3	28.3	4.9	21.6	16.4	294.7	36.1	18.9	3.3	1.049	1.017	0.934	1.031	1.089	1.123	1.128	0.479
V9		36° 48′ 47.8″ S; 70° 40′ 15.1″ W	7	6.49E-02	135.9	53.3	30.0	13.0	353.4	30.6	34.1	14.7	252.1	18.3	25.6	9.4	1.039	1.004	0.957	1.035	1.049	1.086	1.086	0.154
V17		36° 49′ 11.1″ S; 70° 40′ 26.1″ W	6	4.35E-02	119.1	50.6	40.1	4.9	219.8	8.7	39.5	11.9	316.6	38.1	12.9	10.1	1.035	1.014	0.951	1.020	1.067	1.088	1.093	0.524
V4	Qtz-dioritic dyke (Varvarco Tonalite)	36° 48′ 35.8″ S; 70° 40′ 05.4″ W	5	4.74E-02	119.7	38.3	12.0	3.8	329.5	47.7	13.5	3.6	222.1	15.2	10.2	5.6	1.048	1.005	0.946	1.043	1.063	1.108	1.108	0.185
V14	Butalón Tonalite	36° 57′ 46.0″ S; 70° 41′ 12.0″ W	5	3.74E-02	305.5	64.7	6.7	2.8	105.6	24.0	9.0	5.0	199.0	7.6	9.2	4.8	1.037	1.006	0.957	1.031	1.051	1.084	1.084	0.250
V15		36° 58′ 16.3″ S; 70° 40′ 57.7″ W	5	4.39E-02	191.5	14.9	46.7	7.2	64.3	66.2	46.7	15.2	286.5	18.1	15.4	7.1	1.013	1.005	0.982	1.008	1.024	1.032	1.034	0.522
V16		36° 59′ 03.2″ S; 70° 41′ 24.9″ W	5	4.94E-02	129.5	65.0	11.5	2.2	269.2	19.6	15.0	9.2	4.6	14.9	13.5	2.3	1.038	1.005	0.957	1.033	1.050	1.084	1.084	0.202
V5	Radales Aplite	36° 48′ 36.8″ S; 70° 40′ 02.3″ W	5	2.37E-03	152.7	50.6	20.2	7.1	318.2	38.5	20.7	10.2	53.9	7.2	12.0	8.3	1.025	1.004	0.971	1.021	1.033	1.055	1.055	0.220
V10	Jurassic Host Granites	36° 50′ 42.1″ S; 70° 40′ 14.0″ W	5	9.53E-04	120.0	33.5	30.4	12.1	261.7	49.9	46.0	12.7	16.5	19.4	43.6	8.0	1.016	0.998	0.986	1.018	1.013	1.031	1.031	−0.151
V11		36° 50′ 42.1″ S; 70° 40′ 14.0″ W	5	3.16E-02	19.3	40.2	3.0	1.0	154.7	40.1	16.5	2.7	267.0	24.2	16.5	1.4	1.066	0.983	0.951	1.084	1.034	1.121	1.125	−0.420
V12		36° 50′ 46.3″ S; 70° 39′ 45.3″ W	5	2.80E-02	135.5	30.2	22.1	4.1	4.2	48.7	21.8	6.4	241.5	25.4	11.3	3.2	1.015	1.006	0.979	1.009	1.029	1.037	1.039	0.533
V13	Guaracó Norte Fm	36° 50′ 48.5″ S; 70° 39′ 54.5″ W	5	4.40E-04	92.4	63.6	55.2	6.2	331.2	14.5	55.4	10.6	235.3	21.6	15.1	6.0	1.008	1.005	0.987	1.003	1.018	1.021	1.023	0.681

GPS data is given in latitude and longitude. N is the number of samples used in statistics. Km = (K1 + K2 + K3)/3 is the mean magnetic susceptibility (SI units). L is the magnetic lineation (K1/K3); F is the magnetic foliation (K2/K3); P is the degree of anisotropy (Jelinek, 1981); T = (lnF − lnL)/(lnF + lnL) is the Jelinek's parameter (Jelinek, 1981). K1, K2 and K3 are mean AMS eigenvectors, which represent the maximum, intermediate and minimum susceptibility intensities, respectively. Dec – declination in degrees; Inc – inclination in degrees; C1a and C1b are the semiangles of the major and minor axes of the 95 % confidence ellipse, respectively, calculated by the bootstrap method.

with a voltage of 15 kV, current of 15 nA and acquisition time of 10 s per element, in WDS mode. Silicates and oxides were used for calibration. The standards of the Bureau de Recherches Geologiques et Minières (BRGM) were used to refine the results. The obtained mineral compositions are presented in Table 2.

4. Results

4.a. ASTER data, field observations and petrography

As stated earlier in the text, the Varvarco Intrusives are composed of the Varvarco Tonalite, Radales Aplite and Butalón Tonalite. The Varvarco Tonalite and Radales Aplite are a part of a composite intrusion of ~10 km diameter. The Varvarco Tonalite is located in the outer region; the Radales Aplite forms a small stock along the Chacay creek (Fig. 3a, b). These units intrude the rocks of the Guaracó Norte Formation and the Jurassic Host Granites. ASTER data suggest that the shape of the Varvarco pluton is broadly circular, with a typical normal zoning pattern, more felsic towards the centre of the intrusion, if we consider that the Radales Aplite is located towards the centre of the Varvarco Tonalite.

The shape of the Butalón Tonalite is more irregular; the body has a length of 8 km and is elongated in an E–W direction (Fig. 3a, b). The similar response of pink colours in RGB composition 4 3 1 (Fig. 3a) and yellow (Fig. 3b) in RGB composition 7 4 14 of the Butalón Tonalite to the Varvarco Tonalite reflects the same composition. The results of the petrographic analysis are shown in the QAP diagram (Fig. 4) and a detailed description of the outcrops visited in the field is presented below.

4.a.1. Guaracó Norte Formation

The Guaracó Norte Formation, representing the host rock of the Varvarco Tonalite and Radales Aplite, was investigated along the Chacay, Matancilla, Manzano and Guaracó Norte creeks (Figs 2a, 3a, b, 5a). This formation comprises quartzites affected by low-grade metamorphism. Generally, the metamorphic foliation has a NE–SW to N–S strike and steep dip (80°); steep inclinations were also measured close to the contact with the Varvarco Tonalite. In the Guaracó Norte creek, shales and phyllites strike N–S and have a low dip (22°) towards the east. The pelitic rocks and sandstones of this formation are affected by hornblende-hornfels metamorphism that led to the development of andalusite, biotite, diopside and hornblende. This has been related to the intrusion of the Late Cretaceous Varvarco Tonalite (Giacosa *et al.* 2014).

4.a.2. Jurassic Host Granites

Along the Manzano and Guaracó Norte creeks we discovered a new unit at site V12 (Figs 2a, 3a, b, 5b–e), which we tentatively name the Jurassic Host Granites because it has a 185 ± 3 Ma U–Pb age that was obtained by laser ablation multi-collector inductively coupled plasma mass spectrometry on 12 magmatic zircon crystals (unpub. data). This unit was previously described by Zanettini *et al.* (2001) as part of the Radales Aplite (formerly considered the Radales Granite, see Section 4.a.5). The U–Pb geochronology data of the Jurassic Host Granites are part of a work in progress.

The Jurassic Host Granites enclose xenoliths derived from the Guaracó Norte Formation (Fig. 5d). Dykes of granitic composition that intrude the Guaracó Norte Formation in the Manzano creek (36° 50′ 42.1″ S; 70° 40′ 14.0″ W; site V10 in Table 1) can be assigned to the Jurassic Host Granites as well (Fig. 5c). The Jurassic Host Granites have the same syenogranitic composition (Fig. 4) and graphic texture (Fig. 5e) as the Radales Aplite, making it difficult to differentiate them in the field.

4.a.3. Varvarco Tonalite

Along the Matancilla and Chacay creeks, the Varvarco Tonalite can be observed in excellent exposures (Figs 2a, 5a, 6a–d), which include the contact relationships with the Guaracó Norte Formation host rock and with the intruding Radales Aplite (Fig. 5a). The Varvarco Tonalite is represented by medium- to fine-grained, equigranular to porphyritic tonalites, in which mafic minerals appear concentrated in blocks (Fig. 6a, b). The Varvarco Tonalite also hosts microgranular enclaves of dioritic composition (Fig. 6b–d). They have a fine-grained, equigranular texture and are composed of amphibole, biotite, plagioclase, quartz and opaque minerals. The mafic magma was mixed and partially hybridized, as the enclaves show transitional contacts with the host rock (Fig. 6c). Enclave swarms that grade into disintegrated mafic dykes with different hybridization degrees were also observed (Fig. 6d).

The average modal composition of the Varvarco Tonalite is plagioclase (50 %), quartz (30 %), orthoclase (4 %), amphibole (10 %), biotite (5 %), and titanomagnetite, titanite, apatite and zircon (1 %). Plagioclase crystals are subhedral with complex zoning patterns (Fig. 7a). Incipient sericitic alteration of plagioclase is observed in concentric areas. The observed orthoclase phenocrysts have an oikocrystic texture with amphibole and plagioclase inclusions (Fig. 7b). Amphibole is present as subhedral poikilitic megacrysts of nearly 2 cm length that contain plagioclase inclusions. In some areas these large amphibole crystals give the rocks a porphyritic appearance. Subhedral biotite is pleochroic from light to dark brown, and mostly fresh (Fig. 7c, d). Quartz is interstitial and contains inclusions of amphibole. Apatite is frequently acicular. All observed textures are magmatic; grain boundaries are straight, especially between plagioclase and orthoclase (Fig. 7b). Locally, polygonal contacts between quartz grains are observed, suggesting that static recrystallization has occurred.

Late aplitic veins of granitic composition (Fig. 6a) intrude the Varvarco Tonalite in the Chacay creek area (orientations: 285°/75° ENE, 320°/65° ENE). Disintegrated porphyritic quartz-dioritic dykes also cross-cut the Varvarco Tonalite in the Chacay creek area (Fig. 8a). The dykes have poikilitic amphibole and plagioclase phenocrysts in a granular groundmass that is composed of plagioclase, amphibole, biotite, quartz and opaque minerals (Fig. 8b). Amphibole has inclusions of plagioclase and rounded quartz (Fig. 8c). Quartz ‘ocelli’ with reaction rims of amphibole and opaque minerals were occasionally observed (Fig. 8d).

4.a.4. Butalón Tonalite

This intrusive body crops out in the Butalón Norte area, ~15 km to the south of the Varvarco locality (Figs 2a, 3a, b). In the RGB compositions of Figure 3, the Butalón Tonalite is well distinguished from the hosting Permo-Triassic Choiyoi Group. Many granitic dykes and veins of steep to moderate dips and NW to NE strike cross-cut the Butalón Tonalite. They have highly variable widths of between 5 and 50 cm (Fig. 9a). The Butalón Tonalite is classified as a fine-grained tonalitic rock with an average composition of plagioclase (63 %), quartz (23 %), amphibole, biotite (12 %), orthoclase (2 %) and minor euhedral opaque minerals and acicular apatite (Fig. 4). Mafic microgranular enclaves of dioritic composition are present in this facies as well (Fig. 9b). Amphibole (hornblende determined optically) tends to form poikilitic phenocrysts with plagioclase and biotite inclusions (Fig. 9c). Plagioclase has complex zoning and many plagioclase cores are altered to sericite.

Table 2a. Plagioclase compositions analysed by electron microprobe in the Varvarco Tonalite

Mineral	Pl	Pl	Pl	Pl	Pl	Pl	Pl	Pl	Pl	Pl	Pl	Pl	Pl	Pl
Analysis	9	10	21	22	25	26	27	28	31	32	33	34	35	36
Texture	rim	centre	rim	centre	centre	centre	rim	rim	rim	centre	centre	centre	centre	centre
SiO_2	59.32	56.99	60.05	54.44	52.57	52.87	52.91	58.91	57.07	55.46	55.95	55.99	54.18	53.53
TiO_2	b.d.l.	0.02	0.02	b.d.l.	0.03	b.d.l.	b.d.l.	b.d.l.	b.d.l.	0.01	0.03	0.03	b.d.l.	b.d.l.
Al_2O_3	24.73	26.62	24.48	28.08	29.31	29.15	29.19	25.68	26.79	28.12	27.38	27.07	28.09	28.75
Cr_2O_3	b.d.l.	b.d.l.	b.d.l.	b.d.l.	b.d.l.	b.d.l.	b.d.l.	b.d.l.	0.05	b.d.l.	0.03	b.d.l.	0.01	0.05
NiO	b.d.l.	0.06	b.d.l.	0.04	0.02	b.d.l.	b.d.l.	b.d.l.	b.d.l.	b.d.l.	b.d.l.	b.d.l.	0.01	b.d.l.
FeO_t	0.21	0.14	0.26	0.39	0.14	0.17	0.19	0.16	0.18	0.18	0.18	0.17	0.17	0.14
MnO	0.01	0.01	b.d.l.	0.05	b.d.l.	0.01	0.01	0.01	0.01	0.01	b.d.l.	b.d.l.	b.d.l.	0.02
MgO	0.02	b.d.l.	b.d.l.	b.d.l.	b.d.l.	b.d.l.	0.01	b.d.l.	0.02	0.01	b.d.l.	b.d.l.	b.d.l.	0.01
CaO	7.11	9.11	6.35	11.03	12.46	12.40	12.24	7.69	8.68	10.42	9.84	9.73	10.95	11.35
Na_2O	7.53	6.45	7.90	5.38	4.57	4.74	4.66	7.24	6.58	5.78	5.90	5.99	5.39	5.11
K_2O	0.36	0.26	0.44	0.20	0.15	0.15	0.16	0.32	0.23	0.24	0.33	0.29	0.26	0.22
TOTAL	99.37	99.78	99.50	99.78	99.32	99.62	99.48	100.06	99.66	100.31	99.70	99.31	99.17	99.23
xAN	33.61	43.18	30.01	52.48	59.60	58.62	58.65	36.33	41.61	49.24	47.05	46.52	52.10	54.43

Mineral	Pl	Pl	Pl	Pl	Pl	Pl	Pl	Pl	Pl	Pl	Pl	Pl	Pl	Pl	Pl	Pl	Pl	Pl
Analysis	37	38	39	40	41	42	43	44	45	46	59	60	66	67	71	73	74
Texture	centre	centre	rim	centre	centre	centre	centre	centre	centre	centre	centre	rim	centre	rim	rim	rim	centre
SiO_2	55.05	54.34	59.03	56.32	52.01	55.35	54.76	55.80	55.41	56.54	53.25	56.55	47.90	56.36	56.42	55.68	53.65
TiO_2	b.d.l.	0.01	b.d.l.	b.d.l.	b.d.l.	b.d.l.	0.02	0.01	b.d.l.	b.d.l.	0.01	0.02	0.02	0.02	b.d.l.	b.d.l.	0.03
Al_2O_3	28.65	28.61	25.19	26.68	30.20	27.75	28.02	27.68	27.94	27.01	29.05	26.85	32.50	27.74	27.07	27.07	26.99
Cr_2O_3	b.d.l.	0.01	b.d.l.	b.d.l.	b.d.l.	0.01	0.01	0.01	0.02	b.d.l.	b.d.l.	0.01	b.d.l.	0.01	b.d.l.	b.d.l.	b.d.l.
NiO	b.d.l.	b.d.l.	b.d.l.	0.02	b.d.l.	b.d.l.	b.d.l.	b.d.l.	b.d.l.	b.d.l.	0.01	b.d.l.	0.04	b.d.l.	0.04	0.07	0.04
FeO_t	0.15	0.21	0.16	0.16	0.15	0.11	0.16	0.17	0.17	0.21	0.21	0.31	0.17	0.26	0.22	0.19	0.15
MnO	b.d.l.	0.04	b.d.l.	b.d.l.	b.d.l.	0.01	b.d.l.	0.02	b.d.l.	0.02	b.d.l.	b.d.l.	0.02	0.02	b.d.l.	b.d.l.	b.d.l.
MgO	0.01	0.02	0.01	b.d.l.	b.d.l.	b.d.l.	0.01	0.01	b.d.l.	0.01	0.01	0.01	0.01	b.d.l.	0.01	0.01	0.01
CaO	11.10	11.19	7.63	9.48	13.50	10.55	10.74	10.36	10.25	9.50	11.93	9.06	16.01	9.39	9.45	9.31	10.57
Na_2O	5.39	5.17	7.33	6.12	3.88	5.54	5.57	5.91	5.79	6.14	4.88	6.48	2.41	6.17	6.11	6.10	5.18
K_2O	0.22	0.19	0.24	0.27	0.13	0.22	0.22	0.24	0.19	0.25	0.17	0.23	0.08	0.18	0.26	0.19	0.21
TOTAL	100.62	99.93	99.68	99.16	99.99	99.62	99.58	100.32	99.84	99.77	99.57	99.57	99.26	100.16	99.65	98.71	96.89
xAN	52.56	53.87	36.02	45.40	65.33	50.63	50.94	48.55	48.89	45.45	56.90	43.05	78.23	45.23	45.40	45.26	52.34

b.d.l. – below detection level

Table 2b. Amphibole compositions analysed by electron microprobe in the Varvarco Tonalite

Mineral	Amp	Amp	Amp	Amp	Amp	Amp	Amp	Amp	Amp	Amp	Amp	Amp	Amp	Amp	Amp	Amp	Amp	Amp	Amp	Amp	Amp
Analysis	2	3	4	5	6	13	14	16	47	48	49	50	54	55	56	61	62	63	65	68	70
Texture	rim	centre	centre	centre	rim			centre	centre	centre	rim	rim	rim	centre	centre	centre	centre	centre	centre	centre	rim
SiO_2	50.36	48.50	49.33	51.13	49.59	50.77	52.85	53.83	43.37	43.64	51.08	53.53	45.54	44.51	43.84	48.09	48.40	44.60	48.34	44.61	46.33
TiO_2	0.40	0.65	0.43	0.33	0.36	0.22	0.16	0.12	1.61	1.69	0.16	0.09	0.66	1.12	1.65	0.96	1.03	1.64	1.16	1.66	0.65
Al_2O_3	3.85	5.30	4.42	3.69	4.12	3.65	1.80	1.26	8.45	8.39	2.55	1.20	6.61	7.74	8.17	6.15	6.20	8.36	6.23	8.63	6.56
Cr_2O_3	0.02	0.01	0.02	0.03	0.01	b.d.l.	0.04	0.03	b.d.l.	b.d.l.	0.04	0.03	b.d.l.	b.d.l.	0.04	0.03	0.03	b.d.l.	0.03	b.d.l.	b.d.l.
NiO	b.d.l.	0.04	b.d.l.	0.06	b.d.l.	b.d.l.	b.d.l.	b.d.l.	b.d.l.	0.05	0.02	0.06	0.06	b.d.l.	b.d.l.	0.04	0.01	b.d.l.	b.d.l.	b.d.l.	b.d.l.
FeO_t	17.38	17.63	17.96	16.01	15.43	16.30	14.41	12.60	17.62	17.66	16.07	11.97	18.34	17.84	17.37	14.50	14.10	15.15	14.04	17.51	18.11
MnO	1.66	1.57	2.15	1.73	1.34	1.68	1.62	1.37	1.02	0.95	1.67	1.34	1.24	1.04	0.94	0.69	0.73	0.69	0.79	0.89	1.06
MgO	13.46	12.42	12.72	13.77	13.23	13.51	15.01	15.66	10.33	10.44	14.10	15.99	10.53	10.26	10.60	13.76	14.04	12.33	14.06	10.95	10.97
CaO	10.21	10.64	9.45	10.98	11.93	11.29	11.17	12.05	11.27	11.36	10.67	11.46	11.29	11.24	11.33	11.42	11.08	10.80	11.10	11.24	11.46
Na_2O	0.55	0.75	0.58	0.48	0.42	0.40	0.20	0.18	1.19	1.04	0.33	0.13	0.77	0.95	0.99	0.93	1.06	1.44	0.83	1.22	0.79
K_2O	0.28	0.42	0.29	0.25	0.25	0.24	0.08	0.06	0.76	0.72	0.13	0.06	0.63	0.86	0.73	0.42	0.35	0.48	0.41	0.64	0.54
TOTAL	98.26	97.97	97.39	98.52	96.79	98.10	97.45	97.21	95.64	96.03	96.87	95.92	95.79	95.59	95.73	97.08	97.14	95.60	97.08	97.47	96.52
Geothermometers (°C)																					
Ridolfi *et al.* (2010) – Eqn. 1	773	800	750	752	717	742	703	672	841	837	837	734	774	808	831	772	769	836	779	835	771
Ridolfi & Renzulli (2012) – Eqn. 2	343	459	313	470	774	515	449	550	876	851	414	464	821	830	850	782	807	872	808	860	787
Amph-only: Putirka (2016) – Eqn. 5	666.26	699.34	668.48	668.90	682.23	663.59	639.80	642.81	791.41	785.93	645.44	641.23	716.56	753.23	781.33	749.50	755.59	813.07	752.52	791.86	716.61
Geobarometers (kbar)																					
Ridolfi *et al.* (2010) – Eqn. 4	0.5	0.7	0.6	0.5	0.5	0.5	0.3.	0.2	17	17	0.3	invalid	11	14	16	9	9	16	9	17	10
Ridolfi & Renzulli (2012) – average between Eqn. 1a and Eqn. 1b	1.1	1.4	2.3	1	0.7	0.9	0.6	0.4	2	1.7	0.7	0.4	1.3	1.6	1.6	0.9	1.1	1.9	1	1.9	1.1

b.d.l. – below detection level

Table 2c. Biotite compositions analysed by electron microprobe in the Varvarco Tonalite

Mineral	Bt	Bt	Bt	Bt	Bt	Bt	Bt	Bt	Bt	Bt	Bt	Bt	Bt	Bt
Analysis	1	8	12	17	20	23	30	52	53	58	64	69	72	75
Texture	centre	centre	centre	centre	centre	centre	centre	centre	centre	*	*	centre	*	*
SiO_2	35.95	36.51	35.98	36.07	36.10	36.28	35.87	36.03	34.11	36.36	35.94	35.93	35.34	36.15
TiO_2	3.62	3.83	3.52	2.67	3.21	3.77	4.00	3.36	4.66	4.06	4.09	3.46	3.84	3.99
Al_2O_3	13.62	14.55	14.01	14.12	14.01	13.82	13.87	13.62	13.21	13.82	13.35	13.84	13.48	13.60
Cr_2O_3	0.04	0.03	0.02	0.04	b.d.l.	0.03	0.01	b.d.l.	0.02	b.d.l.	b.d.l.	b.d.l.	b.d.l.	b.d.l.
NiO	0.02	0.01	b.d.l.	b.d.l.	0.03	0.08	b.d.l.	0.02	b.d.l.	0.03	0.01	0.01	0.09	b.d.l.
FeO_t	19.65	18.70	19.63	19.64	20.27	19.68	20.77	20.56	20.66	18.62	17.84	20.60	20.49	17.88
MnO	0.81	0.81	0.69	0.82	0.70	0.72	0.72	0.60	0.58	0.31	0.38	0.63	0.50	0.29
MgO	11.33	11.40	11.50	12.00	11.44	11.48	10.65	11.23	9.96	12.29	12.35	11.07	10.90	12.76
CaO	0.04	0.06	0.01	0.04	0.02	0.03	0.08	0.02	1.16	0.03	0.04	b.d.l.	0.02	0.04
Na_2O	0.08	0.09	0.08	0.10	0.09	0.08	0.08	0.10	0.09	0.15	0.14	0.11	0.11	0.19
K_2O	9.43	9.64	9.65	9.63	9.52	9.47	9.24	9.43	8.63	9.50	9.20	9.61	9.57	9.05
P_2O_5	b.d.l.	b.d.l.	b.d.l.	0.02	b.d.l.	b.d.l.	0.01	0.01	0.03	b.d.l.	b.d.l.	b.d.l.	b.d.l.	b.d.l.
TOTAL	94.59	95.63	95.09	95.15	95.39	95.43	95.29	94.97	93.11	95.18	93.33	95.25	94.34	93.95
T(°C) (Henry *et al.* 2005)	728.14	733.13	723.56	689.18	709.61	732.41	733.47	715.09	744.45	746.37	753.34	717.22	731.73	751.74

*Small crystal included in amphibole. b.d.l. – below detection levelTemperatures are calculated with the geothermometer of Henry *et al.* (2005).

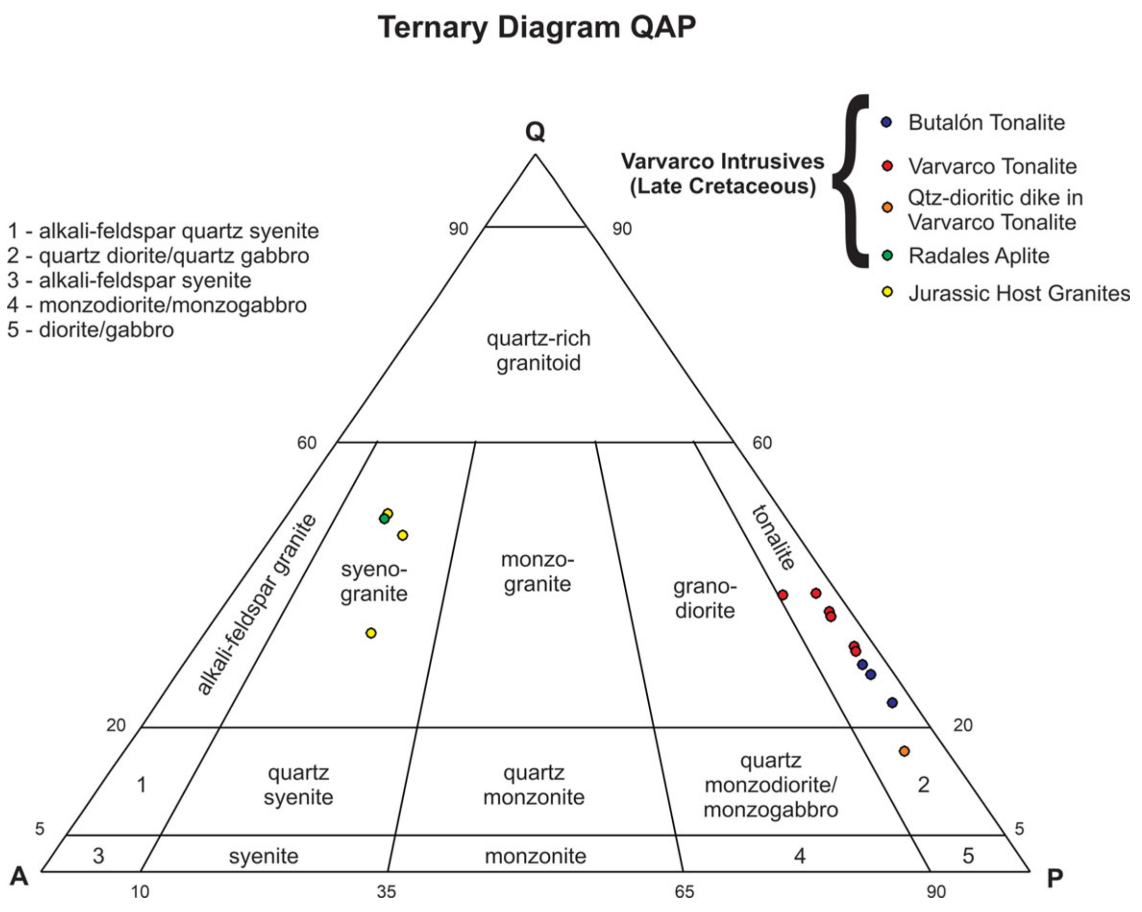

Fig. 4. (Colour online) QAP ternary diagram for the Varvarco Intrusives and Jurassic Host Granites.

GUARACÓ NORTE FORMATION, JURASSIC HOST GRANITES AND VARVARCO INTRUSIVES

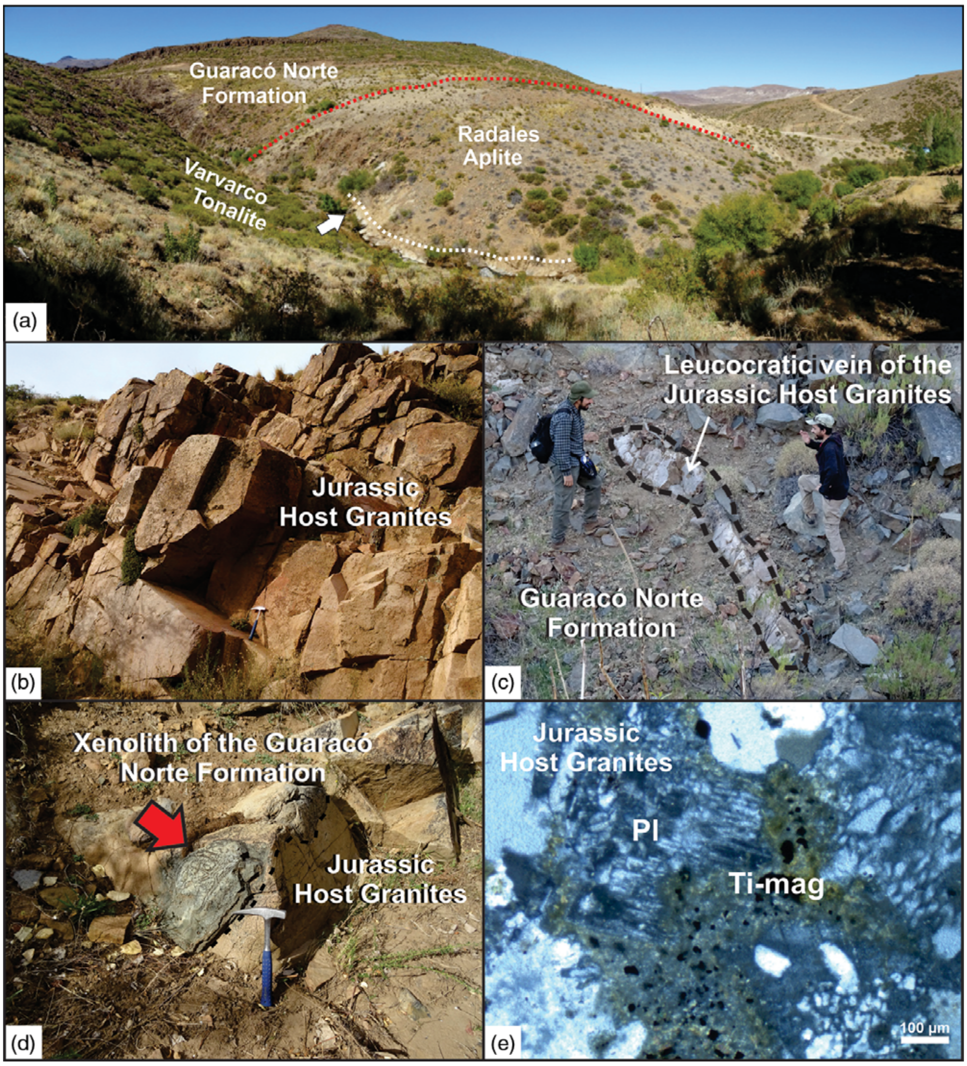

Fig. 5. (Colour online) Outcrops of the Guaracó Norte Formation, Jurassic Host Granites and Varvarco Intrusives. (a) View towards the SE from Puesto Hernández, Chacay creek area, with the outcrops of the Varvarco Tonalite, Radales Aplite and the Guaracó Norte Formation. (b) Outcrops of the Jurassic Host Granites in the Manzano creek area. (c) Leucocratic dyke assigned to the Radales Aplite in the Manzano creek area. (d) Xenolith of Guaracó Norte Formation in the Jurassic Host Granites. Length of hammer for scale is XX cm. (e) Plagioclase phenocrysts in granophyric matrix for the Jurassic Host Granites (cross-polarized light).

Orthoclase is interstitial. Opaque minerals, amphibole and biotite are concentrated in blocks (Fig. 9d).

4.a.5. Radales Aplite

The Radales Aplite crops out only along the Chacay creek (Figs 2a, 5a, 8e). In the satellite image of Figure 3b, the Radales Aplite is shown in yellow owing to its high silica content. The quartz-rich composition of the Guaracó Norte Formation is shown with a very similar colour, making these two units, which were relatively easy to distinguish in the field (red line in Fig. 5a), not clearly separated in terms of composition (Fig. 3b). Therefore, the boundary was highlighted by a dotted line with question marks (Fig. 3a, b).

The contact between the Radales Aplite and the Guaracó Norte Formation is distinctive (Fig. 8e). The Radales Aplite has a fine-grained to aplitic texture and a syenogranitic composition (Fig. 4). Plagioclase phenocrysts (12 %) are immersed in a granophyric matrix formed of quartz (43 %) and orthoclase (40 %) (Fig. 8f). The Radales Aplite is considered a late stage of the Varvarco Intrusives because late leucocratic veins intrude the Varvarco Tonalite (Fig. 6a) and the Butalón Tonalite (Fig. 9a), and these veins could correlate with the small stock cropping out along the Chacay creek (Fig. 5a).

4.b. Plagioclase, amphibole and biotite compositions for the Varvarco Tonalite

Electron microprobe analyses of plagioclase, amphibole and biotite from the Varvarco Tonalite are presented in Table 2.

Plagioclase compositions were calculated based on a 32 oxygen formula unit (Table 2a). Plagioclases are labradorite–andesine or andesine (Fig. 10a–c; Table 2a). They show oscillatory zoning with a decreasing anorthite component (An_{60-30}) from core to rim (Fig. 10a). In some profiles, plagioclase shows a slight increase in An_{45-51} from the core to more external zones and a labradoritic spike of An_{65} separating an external rim of An_{45-30} (Fig. 10b). These compositional spikes correspond to the inner rings observed in many crystals of the Varvarco Tonalite (Fig. 7a). In plagioclases included in amphibole, cores with an anorthite content of up to An_{78} were found.

Amphibole structural formulae were calculated based on a 23 oxygen formula unit and with all Ca in the M4 site (Dale *et al.* 2005; Table 2b). Calcic amphibole compositions were obtained, with $Fe_t/(Fe_t + Mg)$ in the 0.30–0.49 range, and low to moderate TiO_2 contents (0.09 to 1.69 wt %, and 0.01 to 0.19 atoms per formula unit (apfu), respectively). Amphibole cores are mostly magnesiohornblende, whereas amphibole rims are magnesiohornblende to actinolite

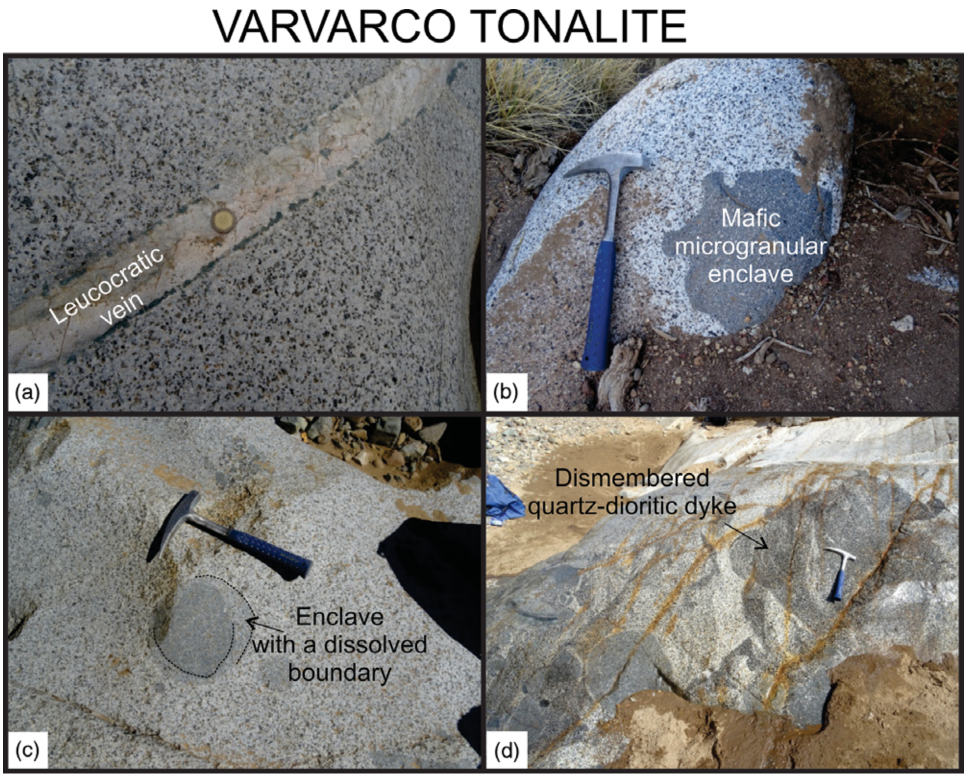

Fig. 6. (Colour online) Outcrop images of the Varvarco Tonalite. (a) Thin leucocratic vein intruding the Varvarco Tonalite in the Chacay
AQ7 creek area. Diameter of coin for scale is XX cm. (b) Mafic microgranular enclave. (c) Partially dissolved (corroded) enclave in a hybrid magma of the Varvarco Tonalite. (d) Disintegrated quartz-dioritic dykes in the Varvarco Tonalite, where different degrees of hybridization are observed.
AQ8 Length of hammer for scale is XX cm.

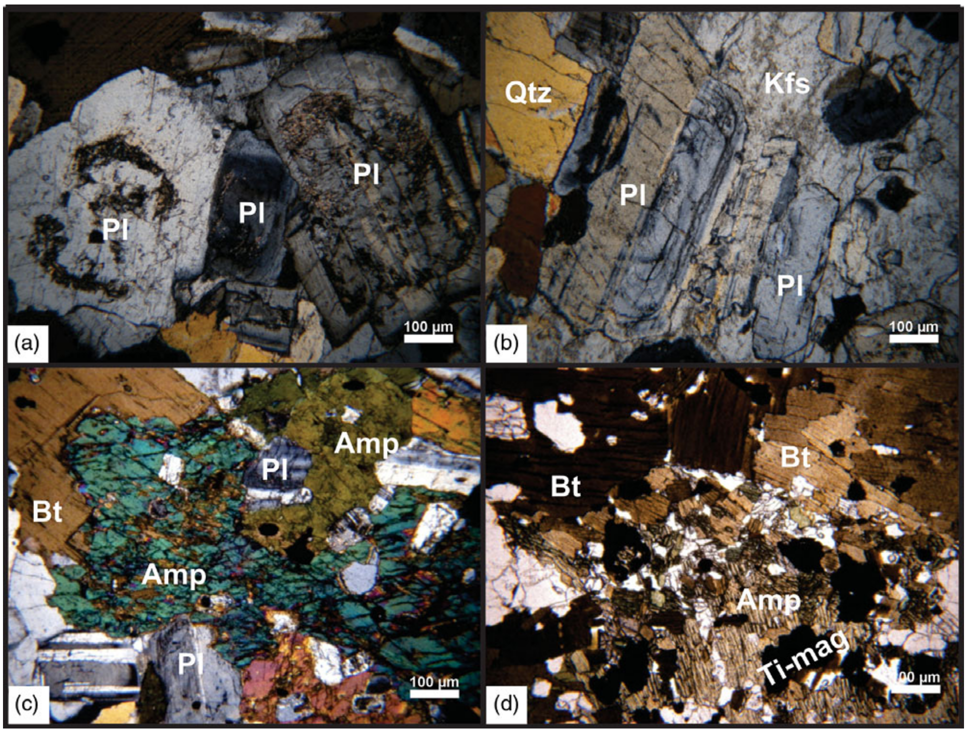

Fig. 7. (Colour online) Petrographic images of the Varvarco Tonalite in cross-polarized light. (a) Plagioclase (Pl) with cores of more calcic composition and lighter rims of more sodic composition. (b) Euhedral plagioclase crystals included in anhedral K-feldspar (Kfs; orthoclase) crystals. (c) Euhedral plagioclase and subhedral amphibole (Amp) and biotite (Bt). (d) Biotite, amphibole and titanomagnetite (Ti-mag) concentrated in blocks in the Varvarco Tonalite. Other mineral abbreviations: Qtz – quartz.

(Fig. 10c–e). All amphiboles balance the Al tetrahedral site occupancy by both tschermakitic and edenitic substitutions (Fig. 10f).

Compositions of fresh biotite are shown in Figure 10d. In order to calculate the biotite formula, we used the method of Li *et al.* (2020). Most biotites are eastonites close to the boundary with phlogopites, with only one biotite (sample 53) falling into the siderophyllite field (Fig. 11a). $Fe_t/(Fe_t + Mg)$ ratios vary between 0.44 and 0.58, and aluminium contents vary between 13.21 and 14.55 wt % Al_2O_3 (Table 2c). In the diagram of Foster (1960) and in the trioctahedral Tischendorf *et al.* (1997) diagram, the analysed grains are classified as Mg-biotites (Fig. 11b, c), with biotite from sample 53 falling into the Fe-biotite field (Fig. 11c). In the ternary diagram of Nachit *et al.* (2005), the compositions are compatible with primary and re-equilibrated primary biotites (Fig. 11d).

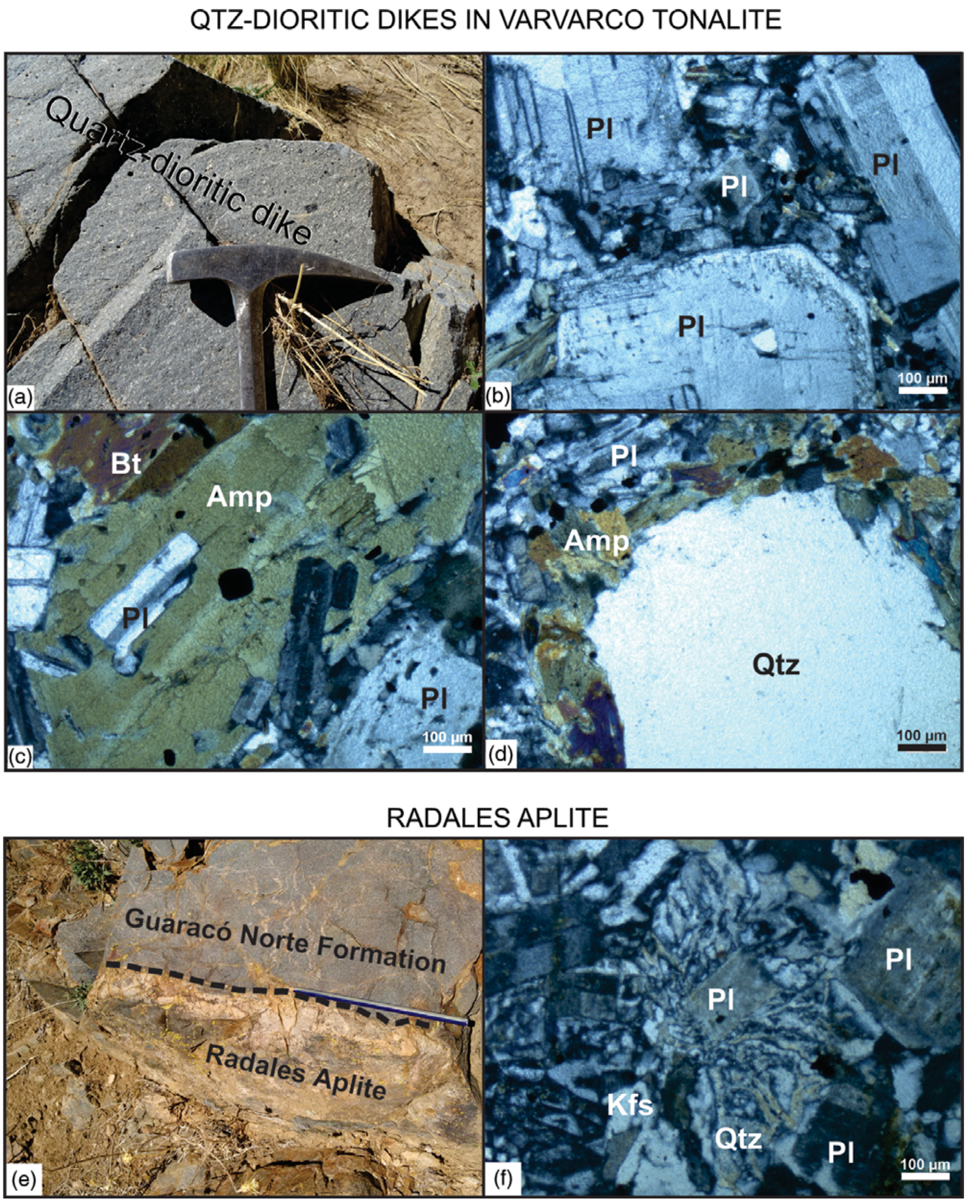

Fig. 8. (Colour online) Quartz-dioritic dykes intruding the Varvarco Tonalite and Radales Aplite. (a) Fine-grained texture of a quartz-dioritic dykes. Width of hammer head for scale is XX cm. (b) Plagioclase phenocrysts in a fine-grained matrix mainly composed of plagioclase. (c) Amphibole phenocryst with inclusions of plagioclase and opaque minerals. (d) Rounded quartz xenocryst rimmed by amphibole and opaque minerals (quartz ocelli). (e) Contact between the Radales Aplite and the hosting Guaracó Norte Formation. Length of pencil for scale is XX cm. (f) Xenolith of Guaracó Norte Formation in the Radales Aplite. Mineral abbreviations as in Figure 7.

AQ9 AQ10

Given that biotite is prone to secondary alteration, Ti was proposed to act as a discriminator, with Ti content <0.55 Ti per 22 oxygen formula unit indicative of fresh magmatic biotite (e.g. Li *et al.* 2017). Varvarco biotites contain 2.6–4.66 wt % TiO_2, which converts to 0.31–0.56 Ti pfu. Only one biotite grain (sample 53) is above 0.55 Ti pfu, supporting their magmatic origin.

4.c. Anisotropy of magnetic susceptibility (AMS)

As was stated in the introduction, AMS studies are used here to evaluate the timing and possible emplacement mechanisms of the Varvarco Intrusives in relation to regional deformation affecting the Cordillera del Viento range. At all investigated sites, the petrofabric was magmatic, with most minerals of euhedral shape, and no evidence of late solid-state deformation. The AMS ellipsoids for the individual sites obtained for each lithology are presented in online Supplementary Material Figure S1a–e. As a usual practice in AMS studies, mineral and magnetic fabrics are assumed to be parallel. This could only be accomplished for site V8, the only site where we could measure the magmatic foliation in the field, whereas sampling in the other sites was carried out in isotropic rocks.

The corrected anisotropy degree Pj value and the shape parameter T (Jelinek, 1981) can be used to describe the geometry of the magnetic ellipsoid. The general positive correlation between Km and Pj shows that titanomagnetite controls the anisotropy in the three analysed plutonic rocks, at both sample and site scale (online Supplementary Material Figure S1a–f). Most values of the shape parameter T at the site scale lie between −0.5 and 0.5 (online Supplementary Material Figure S1f; Table 1). Thus, the magnetic ellipsoids are predominantly triaxial, with good determinations of K1 and K3 axes corresponding, respectively, to magnetic lineations and poles of foliation planes.

The structural mapping of the Varvarco Intrusives was constructed with the AMS data for each sampling site (magnetic foliation and lineation maps; Fig. 12a, b). The orientation of the metamorphic foliation of the Guaracó Norte Formation taken from Giacosa *et al.* (2014) was also added to complete the

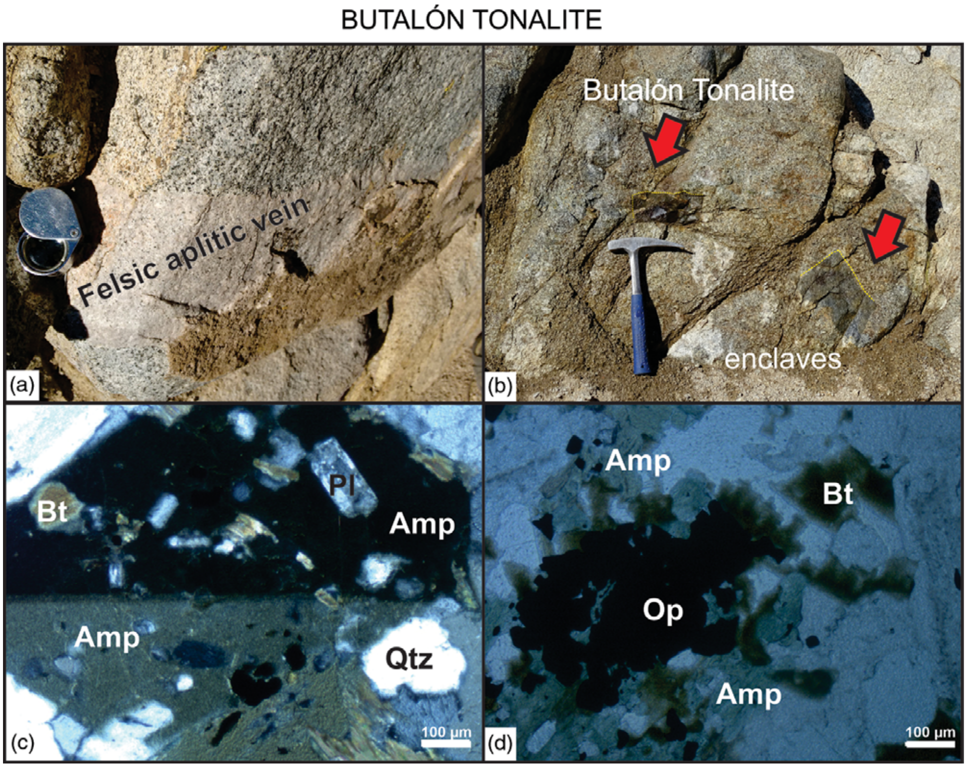

Fig. 9. (Colour online) Outcrops and petrographic images of the Butalón Tonalite in cross-polarized light. (a) Felsic aplitic vein intruding the Butalón Tonalite. Length of hand lens for scale is XX cm. (b) Mafic microgranular enclaves. Length of hammer for scale is XX cm. (c) Amphibole megacryst with inclusions of plagioclase and biotite. (d) Mafic minerals. Mineral abbreviations as in Figure 7 and Op – opaque minerals.

AQ11 AQ12

structural map of the host rock in the Varvarco area (Fig. 12a). In this area, the strike of the magnetic foliation planes of the Varvarco Tonalite oscillates between NNW–SSE and NNE–SSW, and they systematically dip steeply to moderately towards the east (online Supplementary Material Fig. S1a; Fig. 12a). In turn, the magnetic foliation of the Radales Aplite and Jurassic Host Granites is steeply dipping as in the Varvarco Tonalite, but the strike of the magnetic foliation of the Jurassic Host Granites is more variable, especially in the Manzano creek area (online Supplementary Material Fig. S1c, d; Fig. 12a). The Guaracó Norte Formation in the area between the Chacay and Matancilla creeks shows steeply dipping metamorphic foliations in a N–S strike direction, changing to a NW–SE strike (Giacosa *et al.* 2014; Fig. 12a). The foliation obtained for site V13 in the Manzano creek has a steeply dipping NNW–SSE strike
AQ13 (online Supplementary Material Fig. S1e; Fig. 12a).

The average lineations of the Varvarco Tonalite plunge moderately to steeply towards the SE (online Supplementary Material Fig. S1a; Fig. 12b); with one site (V3) with a shallowly plunging lineation trending towards the NW (online Supplementary Material Fig. S1a; Fig. 12b). The lineations of the Radales Aplite and Jurassic Host Granites are more diverse: they plunge moderately towards the SE, but lineations plunging to the NE were also found (online Supplementary Material Fig. S1c, d; Fig. 12b). The lineation found in the Guaracó Norte Formation at site V13 is shallow dip-
AQ14 ping (online Supplementary Material Fig. S1e; Fig. 12b).

The quartz-dioritic dyke at site V4, belonging to the Varvarco Tonalite, has a steeply dipping NW–SE magnetic foliation plane, parallel to dyke strike (online Supplementary Material Fig. S1a). Magnetic lineation plunges moderately to the SE (online Supplementary Material Fig. S1a).

In the area of Butalón Norte, the Butalón Tonalite has steeply dipping magmatic foliation planes with different attitudes; two sites have an E–W strike (V14 and V16), whereas the remaining site (V15) has a N–S strike (online Supplementary Material Fig. S1b). The magnetic lineation is subhorizontal in the case of site V15, and sub-vertical in the case of sites V14 and V16 (online Supplementary Material Fig. S1b).

4.d. Mean susceptibility and minerals responsible for the AMS ellipsoids

The simple exploration of the nominal value of bulk magnetic susceptibility indicates which are the main minerals controlling the magnetic fabric of rocks (Bouchez, 2000). The mean magnetic susceptibilities (Km) of the Varvarco Tonalite and the Butalón Tonalite are 38.56×10^{-3} SI and 43.57×10^{-3} SI, respectively. These values are significantly higher than those for the Radales Aplite of 2.37×10^{-3} SI and the Jurassic Host Granites of 20.18×10^{-3} SI (averages were taken using the data of Table 1). The Guaracó Norte Formation has an even lower Km of 0.44×10^{-3} SI (Table 1). These high bulk susceptibility values, higher than 4×10^{-4} SI in most of the samples of the Varvarco and Butalón plutons, suggest that the AMS signal is dominated by magnetite (following the method of Bouchez, 2000; online Supplementary Material Fig. S2a, b). This is consistent with the mineralogy of the studied granitoids.

Rock magnetic studies can be used to further constrain which minerals dominate the magnetic anisotropy of the rocks. In particular, it is important to determine the domain state of the magnetite, which is essential for the correct interpretation of the magnetic ellipsoids (Grégoire *et al.* 1995; Borradaile & Jackson, 2010). Therefore, hysteresis loops, the anisotropy of isothermal remanence (AIRM) and backfield curves were performed on the Varvarco Tonalite (online Supplementary Material Fig. S2a) and the Jurassic Host Granites (online Supplementary Material Fig. S2b), all in agreement with the presence of magnetite. Magnetite is mostly of pseudo-single-domain (PSD) type, as is suggested by the diagram of Day *et al.* (1977) (Fig. 13). However, two samples from the Varvarco Tonalite have a fine-grained, single-domain (SD)

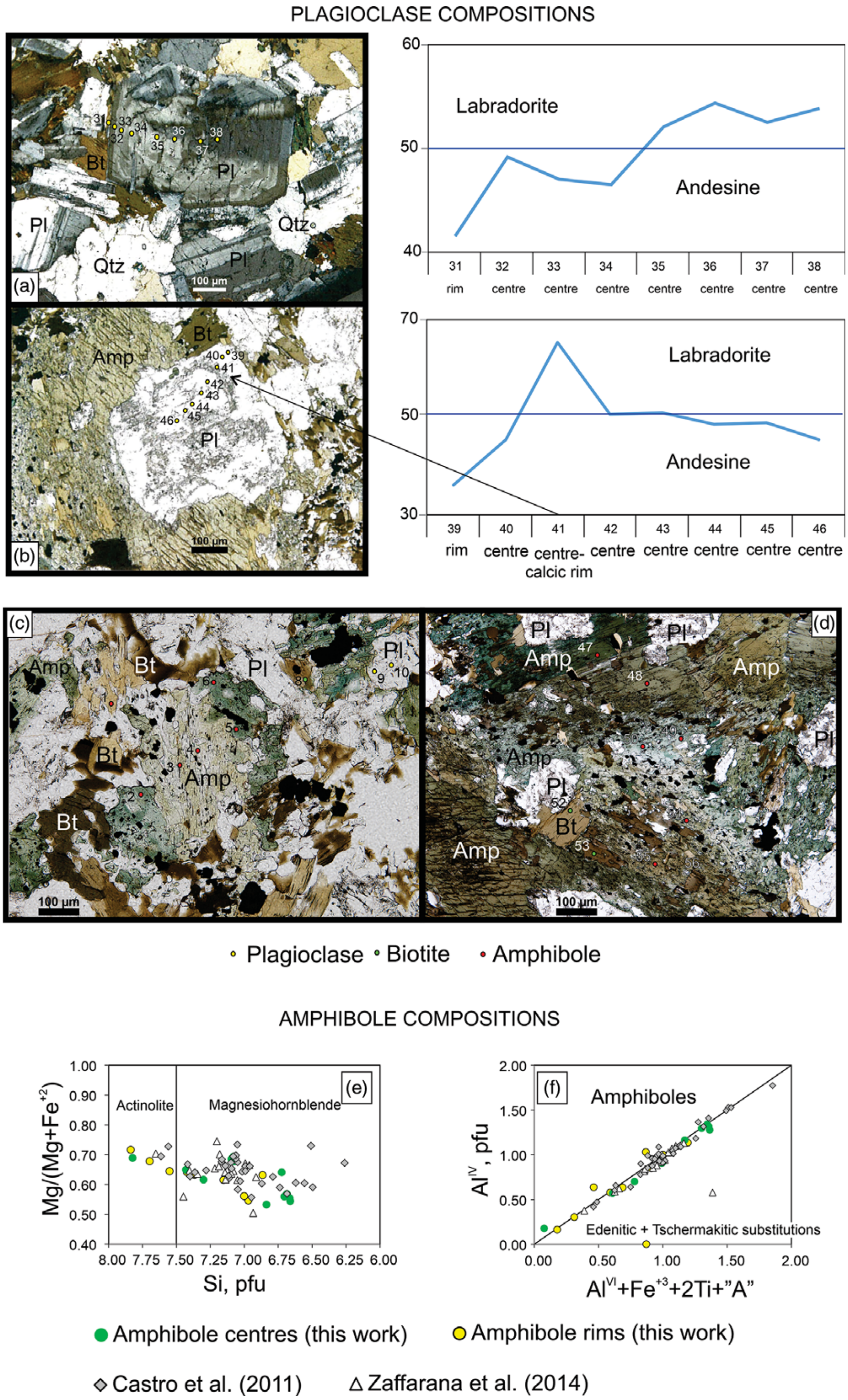

Fig. 10. (Colour online) Plagioclase and amphibole compositional classification. (a, b) Plagioclase zoning profiles for the Varvarco Tonalite. (c, d) Photomicrographs with cross-polarized light showing some analysed spots of amphibole (red), biotite (green) and plagioclase (yellow). (e) Amphibole classification diagrams of Leake *et al.* (1997). (f) Al^{IV} versus $Al^{VI} + Fe^{+3} + 2Ti +$ 'A' graph (Kawakatsu & Yamaguchi, 1987) shows that nearly all amphiboles have a good 1:1 fit between vertical and horizontal axes. This suggests that charge compensation due to the introduction of Al^{IV} was accomplished by both the edenitic and tschermakitic substitutions.

magnetite signature (samples from sites V7 and V8; Fig. 13). Consequently, for these AMS sites, anisotropy of the anhysteretic remanence ellipsoids (AARM) was determined. The coincidence of the AARM and AMS ellipsoids (Fig. 14) further supports that magnetite controls the AMS signal and no axis inversion is necessary owing to the presence of SD magnetite. It can be concluded that the interpretation of the AMS fabric in all sites is direct, as the magnetic lineation coincides with the K1 axis and the pole of the magnetic foliation corresponds to the K3 axis, with the K1 and K3 directions taken from the AMS ellipsoids.

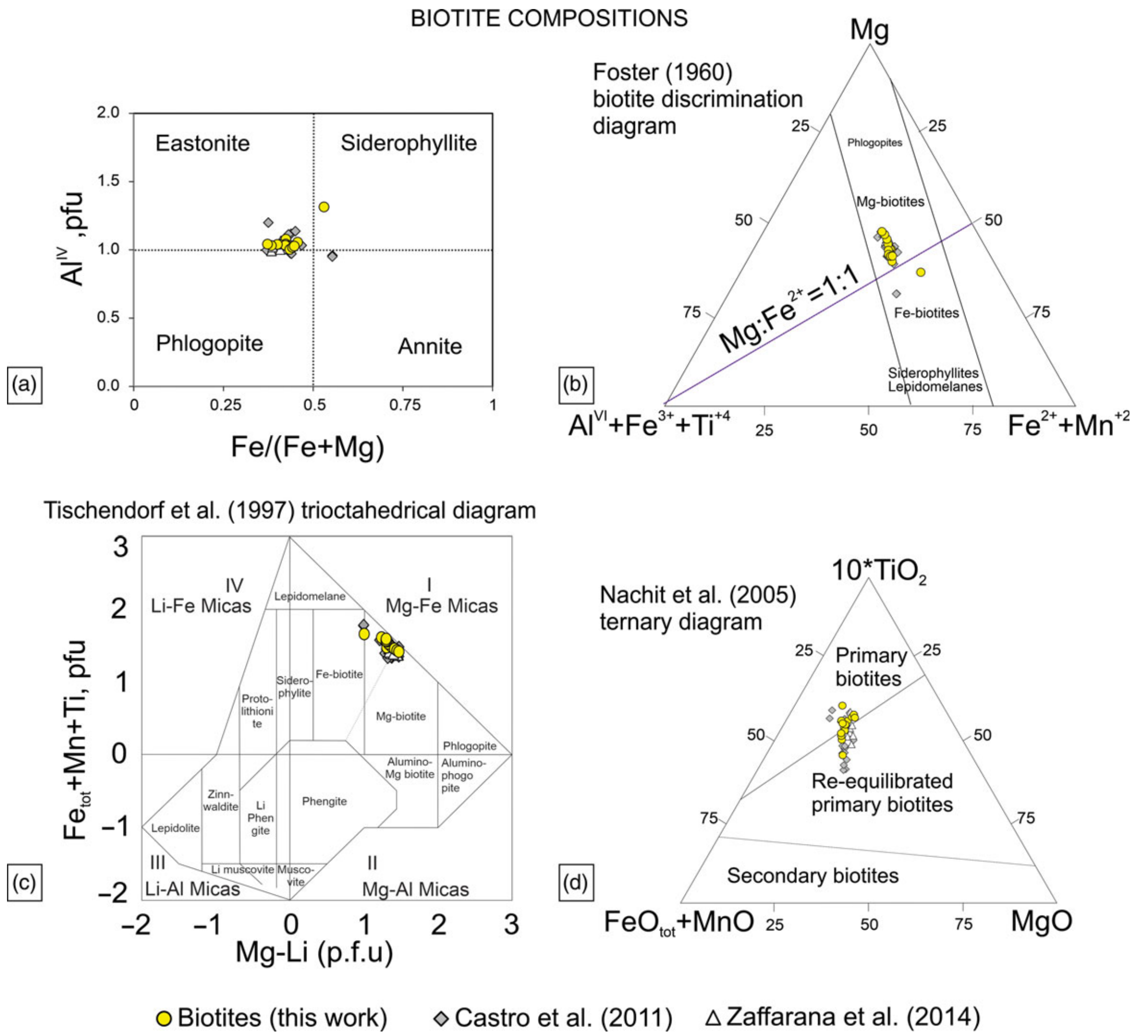

Fig. 11. (Colour online) Biotite compositional classification. (a) Biotite classification (Al^{IV} as a function of its Fe/(Fe + Mg) ratio; Deer *et al.* 2013). (b) Biotite discrimination diagram after Foster (1960). (c) Trioctahedrical classification diagram after Tischendorf *et al.* (1997). (d) Ternary diagram for discriminating between primary magmatic biotites and re-equilibrated and secondary biotites after Nachit *et al.* (2005).

4.e. Apatite fission tracks (AFT) results

Samples VAR5 (36° 48′ 58.7″ S; 70° 40′ 20.2″ W) from the Varvarco Tonalite and BU4 (36° 59′ 03.2″ S; 70° 41′ 24.9″ W) from the Butalón Tonalite were analysed by AFT. For sample VAR5, AFT results were obtained for 21 apatite crystals. In the radial plot, the mean age obtained is 67.5 ± 8.0 Ma (Late Cretaceous; Fig. 15a; Table 3), with low dispersion of ages from individual crystals. This sample passed the chi-square test suggesting that there is a sole age distribution ($P(\chi^2) = 90.72\,\% > 5\,\%$; Galbraith, 1981; Green, 1981). From sample BU4, 13 apatite crystals were measured. The mean age in the radial plot is 50.3 ± 5.9 Ma (early Eocene), with low age dispersion for individual grains (Fig. 15b; Table 3). The sample also passed the chi-square test (44.37 %), suggesting that the single grain ages have a sole age distribution ($P(\chi^2) = 44.37\,\% > 5\,\%$).

5. Discussion

5.a. Magma hybridization processes in the I-type Varvarco and Butalón intrusive bodies

According to the field and petrographic observations presented above, we interpreted that the Varvarco and Butalón tonalites are hybridized igneous bodies that have experienced magma mingling-mixing at their sources. In the area, the more mafic part is represented by the quartz-dioritic dykes, which are intermediate in composition, whereas the more felsic products are represented by the Radales Aplite. The intermediate composition of the quartz-dioritic dykes indicates that the hybridization process was strong in the area.

The presence of enclaves with different degrees of hybridization such as enclaves with distinct contacts with the host tonalite (Fig. 5c) or enclaves partially absorbed (corroded) and rimmed by a new hybrid magma (Fig. 5d), and the varied degree of hybridization observed in enclave swarms (Fig. 5e), suggest that the mingling process would have started before the emplacement (i.e. at the source). Magmatic flow had possibly favoured the incorporation of heterogeneous enclaves such as those shown in Figure 5c–e (e.g. Bateman, 1995). At higher temperatures, mixing processes are likely to have taken place in the magma chamber. A schematic hybridization trend is shown in Figure 16, based on Barbarin's (2005) model.

Increasing crystallization stages of the intermediate host magma (given mainly by the more voluminous tonalite), would produce the magma hybridization textures that are observed, which range from early to late mingling features. Scattered mafic

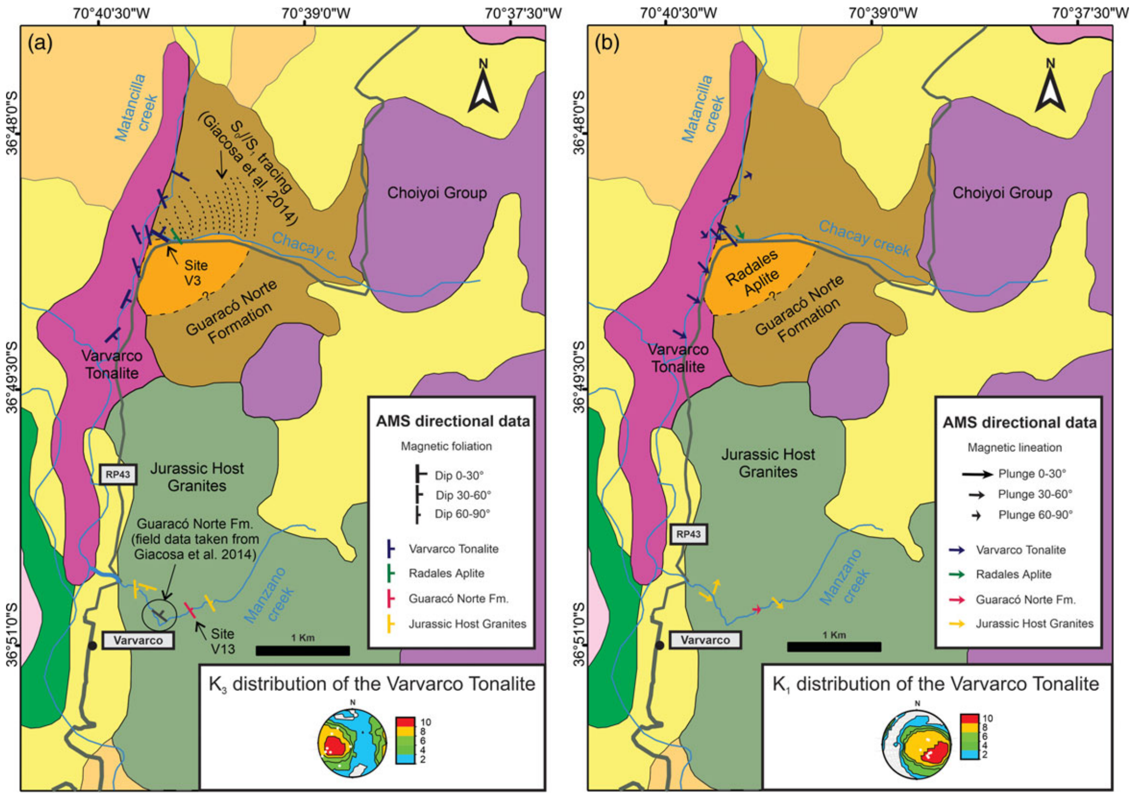

Fig. 12. (Colour online) (a) Map showing magnetic foliation planes (K1–K2 planes), defined as the plane perpendicular to K3 in the Varvarco Tonalite. Inset shows K3 distribution of the magmatic foliations. (b) Map showing magnetic lineation (K1 direction) in the Varvarco Tonalite. Inset shows K1 distribution of the magmatic fabrics. The stereonets represent contoured Kamb equal-area lower-hemisphere stereographic projections made with the software Stereonet 9.9.5 (Allmendinger *et al.* 2012; Cardozo & Allmendinger, 2013). The scale represents Kamb contours in standard deviation.

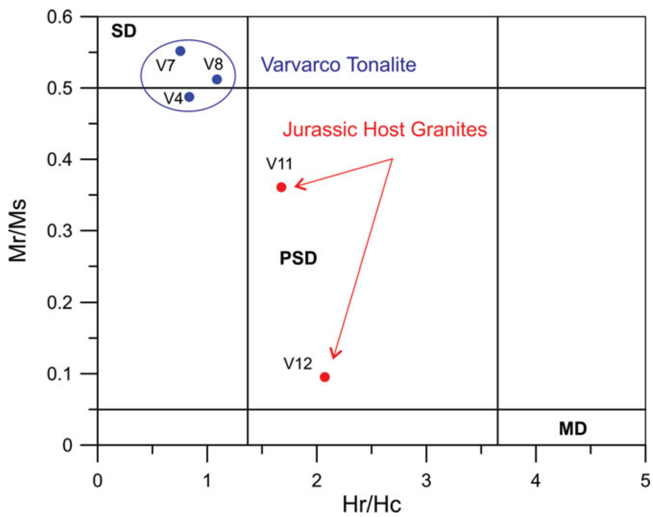

Fig. 13. (Colour online) Domain state of the magnetite of the Varvarco Tonalite and Jurassic Host Granites. Diagram of Day *et al.* (1977). Hc – coercive force; Hr – remanent coercive force; Ms – saturation magnetization; Mr – remanent magnetization; SD – single-domain; PSD – pseudo-single-domain; MD – multidomain.

AQ15

magmatic enclaves from the Varvarco and Butalón plutons represent early mingling textures (Fig. 16a, b), whereas the presence of needle-like apatite in these enclaves points to early mafic magma quenching (Wyllie *et al.* 1962). The lack of chilled margins shown by most of the enclaves suggests that local mixing was caused by partial dissolution of the originally chilled borders (Barbarin, 2005). The presence of outer zones of calcic plagioclase (labradoritic spikes) in more sodic plagioclase of the Varvarco Tonalite (Fig. 10b) has also been interpreted as a result of mixing processes involving coeval acid and mafic magmas (fig. 7b in Hibbard, 1981), and can be due to quenching related to magma hybridization (Mollo *et al.* 2011; Molina *et al.* 2012).

The enclave swarms present in the Varvarco Tonalite represent magma channels that were used by new pulses of magma arriving to the chamber (e.g. Bateman, 1995; Tobisch *et al.* 1997). The disrupted quartz-dioritic dykes (Fig. 16c) suggest that mafic magma intruded through early fractures in the increasingly more crystallized Varvarco Tonalite (Barbarin, 2005).

The presence of K-feldspar and amphibole oikocrysts with inclusions of early formed minerals is evidence of mafic magma undercooling and thermal adjustment (Castro *et al.* 1991). Separate plagioclase crystals constitute chadocrysts included in relatively larger, late amphibole oikocrysts. Chadocrysts remain representatives of an earlier textural development stage (Higgins & Roberge, 2003).

Rounded quartz phenocrysts rimmed by amphibole ('quartz ocelli'; Fig. 8d; Vernon, 1990; Hibbard, 1991) are observed in the dioritic to quartz-dioritic dykes and are assigned to the liquid-dominated hybridization stage (compare Fig. 16a). For quartz ocelli, the parental magma of the quartz-dioritic dykes would have already mixed-mingled by the time it intruded the solidified host rock, suggesting that the hybridization process had been achieved in several stages.

No solid-state recrystallization textures were observed in the Varvarco Intrusives. The only modification of grain boundaries

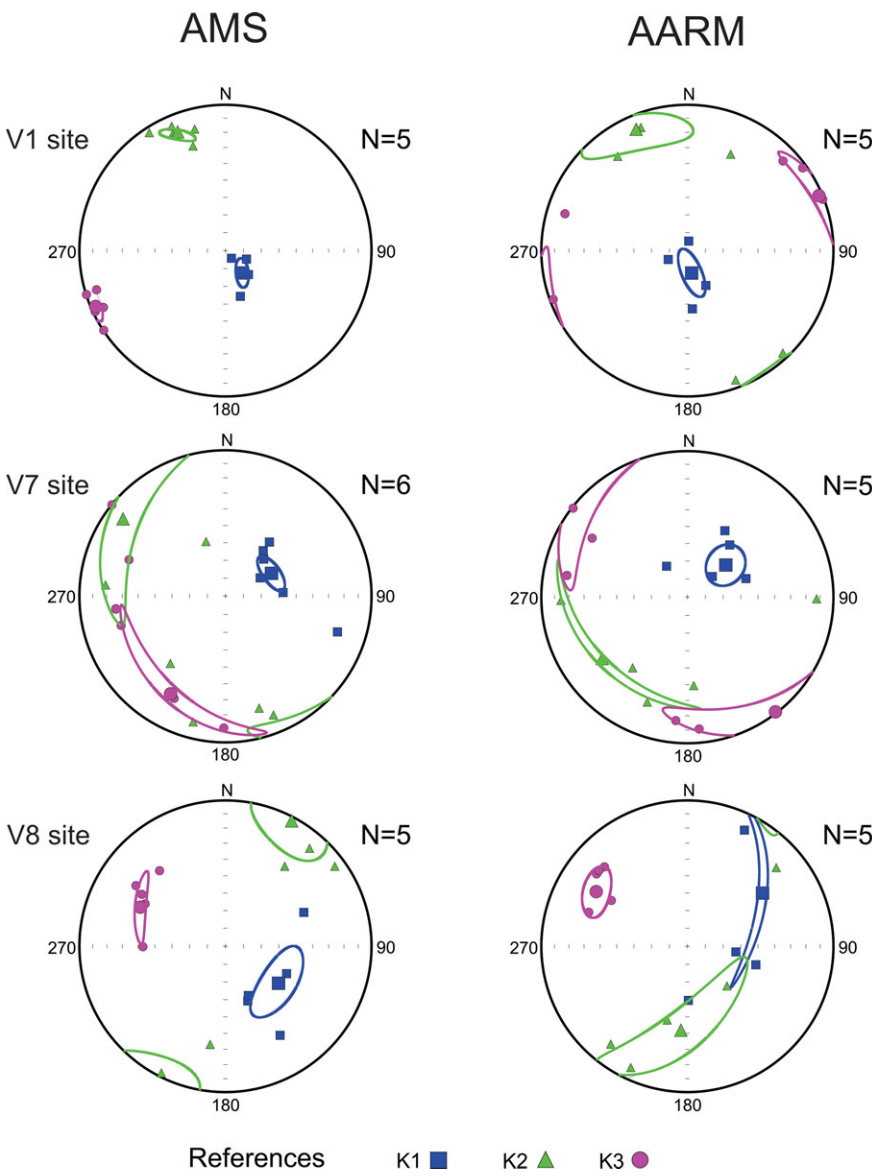

Fig. 14. (Colour online) Comparison of AMS and of AARM ellipsoids showing that magnetite and paramagnetic minerals have fabrics with the same orientations. Equal-area projection in geographic coordinate system.

that was locally observed is some polygonization of quartz grains. This suggests that the rocks underwent some degree of static recrystallization (textural coarsening: Higgins, 2011). The Radales Aplite sample from site V5 sampled for this study has a granophyric texture suggesting that it cooled under shallow subvolcanic conditions (Vernon, 2010).

The affinity of the Varvarco Intrusives with calc-alkaline I-type magmas (Franchini *et al.* 2003; Casé *et al.* 2008) and the predominance of intermediate compositions in the suite, with hornblende as the main mafic mineral, is typical of Cordilleran magmas. These water-rich compositions are characteristic of subduction environments (Bachmann & Bergantz, 2008). Amphibole and biotite crystals from the Varvarco Tonalite crystallized from magmas of calc-alkaline composition (Fig. 17a–f). According to the classification of Molina *et al.* (2009), the amphibole cores and rims crystallized in equilibrium with subalkaline magmas (Fig. 17a–d), although some amphibole cores fall into the field of subalkaline trachytoid magmas (Fig. 17b). Given that the Varvarco area is poorly studied, there are no granitoid rocks in the vicinity to directly compare with the mineralogy of the Varvarco Intrusives. In Figures 10, 11, 17 and 18 we compare the compositions of amphiboles and biotites with the amphiboles and biotites of Zaffarana *et al.* (2014) and Castro *et al.* (2011). Zaffarana *et al.* (2014) reported granitoids of Late Triassic age from the Central Patagonian Batholith at Gastre (North Patagonian Massif) which were emplaced during the early stages of Gondwana break-up. In turn, Castro *et al.* (2011) reported Jurassic granites of the North Patagonian Batholith in the area of Bariloche (North Patagonian Andes) which were, like the Varvarco rocks, formed by the Andean subduction system. The Varvarco amphiboles largely overlap in composition with the amphiboles reported for the Late Triassic granites of the Gastre Superunit of the Central Patagonian Batholith studied by Zaffarana *et al.* (2014) and have less variable TiO_2 concentrations than amphiboles reported for the Jurassic granites of the Patagonian Batholith studied by Castro *et al.* (2011).

The composition of the biotite crystals is comparable to that of calc-alkaline orogenic suites (Fig. 17e, f) in the tectonic discrimination diagram of Abdel-Rahman (1994). The presence of titanomagnetite as the main oxide in these rocks (Varvarco Tonalite; online Supplementary Material Fig. S2a) is also compatible with

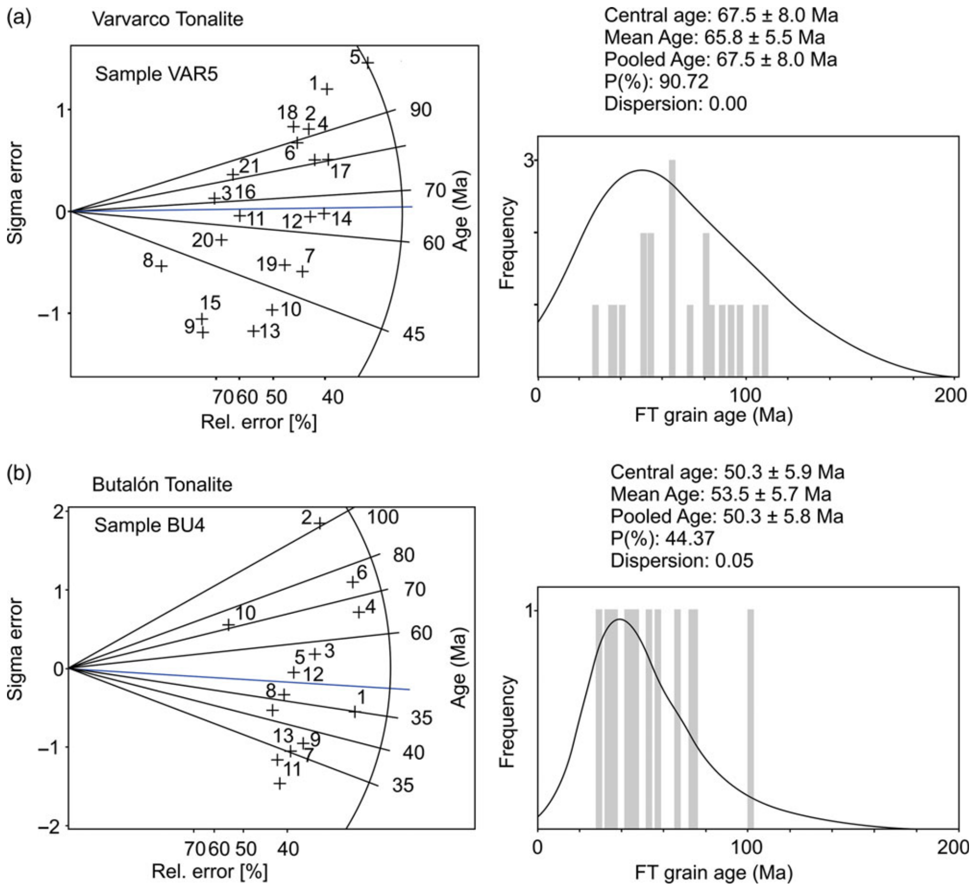

Fig. 15. (Colour online) Apatite fission-track data of samples (a) VAR5 and (b) BU4. Diagrams on the left of the figure show the radial distribution of ages of each grain, where the central age is marked in blue. Diagrams on the right show the frequency histogram for obtained ages.

granites of the magnetite series of Ishihara (1977), in agreement with the results of Casé *et al.* (2008). Similar to the amphiboles, the Varvarco biotites largely overlap in Al_2O_3, MgO and FeO_T concentrations with biotites reported by Zaffarana *et al.* (2014) and Castro *et al.* (2011) (Fig. 17e, f), with the biotites of Castro *et al.* (2011) showing slightly larger variations.

5.b. Parental melt conditions of the Varvarco Tonalite

5.b.1. Thermobarometry

To estimate the magma storage temperatures we used geothermometers based on amphibole–plagioclase compositions (Holland & Blundy, 1994, expression B; Molina *et al.* 2021, expressions A1, A2 and B2), amphibole compositions (Ridolfi *et al.* 2010; Ridolfi & Renzulli, 2012; Putirka, 2016), biotite (Henry *et al.* 2005) and melt compositions (Molina *et al.* 2015; Putirka, 2016). Individual results are presented in Table 2, and a summary is presented in Table 4.

Temperatures obtained with the expressions A1, A2 and B2 from Molina *et al.* (2021) agree reasonably and are between 623 and 703 °C (Table 4). In general, temperatures obtained with expression A1 are lower than those obtained with expressions A2 and B2 (Table 4). In the case of the pressure-dependent expressions A1 and A2, results obtained at 1 and 5 kbar are almost identical (Table 4). For these calculations, we used amphibole compositions 61, 62, 63 and 65, which are from cores of amphibole crystals that satisfy the validation criteria of these geothermometers (Molina *et al.* 2021). These amphibole cores were combined with plagioclases 9, 21, 28 and 39, of andesine composition An_{30-36}, which also pass the validation criteria proposed by the authors (Table 2a, b).

The expression B from the Holland & Blundy (1994) amphibole and plagioclase thermometer was used for the same plagioclase cores as in the Molina *et al.* (2021) geothermometer, and amphibole cores with 0.2 (apfu) Ti and 1.5 (apfu) Al^{IV} contents. This filter yielded a temperature of 716–784 °C for the amphibole cores, and these temperatures agree with the amphibole core-only temperatures (Ridolfi *et al.* 2010; Ridolfi & Renzulli, 2012; Putirka, 2016; Table 2b). However, the higher temperatures could be due to either their high Al^{VI} or low Mg occupancies, and therefore we consider that the crystallization temperatures around 623–703 °C obtained with the expressions from Molina *et al.* (2021) are more likely.

Liquid-only temperatures of Molina *et al.* (2015) and Putirka (2016) for amphibole-saturated magmas are, as expected, higher than the temperatures calculated by using amphibole crystals and by the combination of amphibole and plagioclase crystal cores. They range from 922 to 958 °C (Table 4), and for these calculations the liquid composition was estimated using the whole-rock composition of sample BPN11 from the Varvarco Tonalite (sample reported in Kay *et al.* 2006). The obtained liquid-only temperatures are compatible with the amphibole stability field in subalkaline liquids (see fig. 15 in Molina *et al.* 2009 and fig. 9 in Kiss *et al.* 2014), consistent with a system that involved amphibole-saturated parental melts.

The combination of Ti and Mg/(Mg + Fe) ratios of biotites were used to determine temperature following the method of Henry *et al.* (2005). Biotite compositions are well within the calibration range of the method ($X_{Mg} = 0.275–1.000$, $Ti = 0.04–0.6$ apfu) and yielded temperatures between 689 and 753 °C, in excellent agreement with amphibole temperatures determined by Molina *et al.* (2021) (Table 4).

Table 3. Apatite fission-track data

				Dosimeter		Spontaneous		Induced				Central age (Ma) ± 1s
Sample	Lithology	n	U (ppm)	ρD	*ND*	ρ_S	N_S	ρi	*Ni*	$P(\chi^2)$	Age dispersion	
VAR5	tonalite	21	9.19	8.43	5000	2.61	131	5.61	281	90.72	0	67.5 ± 8.0
BU4	tonalite	13	14.18	8.42	5000	2.95	131	8.48	377	44.37	0.05	50.3 ± 5.8

AQ16

AQ17 Central ages calculated with a calibration of 330.40 ± 20.16 Ma. n – number of measured grains. * Kinetic parameters.

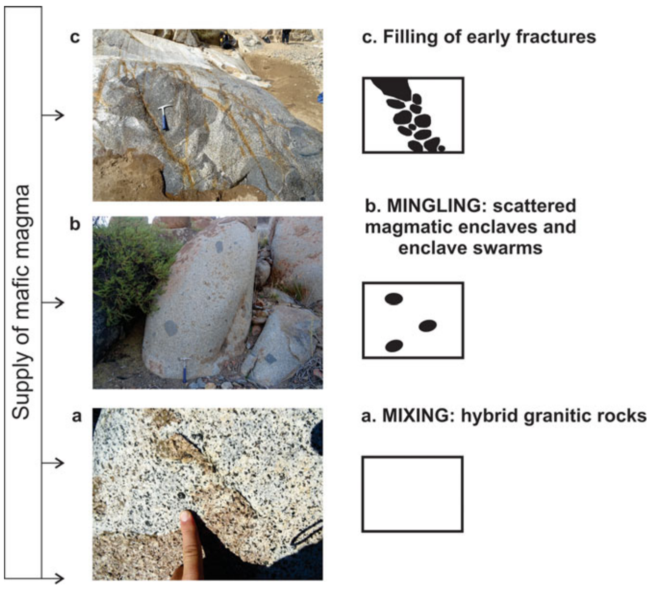

Fig. 16. (Colour online) Schematic magma hybridization processes proposed for the Varvarco Tonalite, based on the model of Barbarin (2005).

Crystallization pressures were estimated using the Ridolfi & Renzulli (2012) amphibole-only geobarometers (average between the results of equations 1a and 1b) and the Molina *et al.* (2015) and Anderson & Smith (1995) amphibole–plagioclase barometers. For these calculations, as in the case of the geothermometers, only amphiboles 63 and 68 and plagioclases 9, 21, 28 and 29 (Table 2a, b) that passed all the validation parameters of Molina *et al.* (2015, 2021) were used. We also estimated pressures using the Al-in-hornblende geobarometers of Hammarstrom & Zen (1986), Hollister *et al.* (1987), Johnson & Rutherford (1989) and Schmidt (1992) (Table 4).

The highest pressures were calculated using the Schmidt (1992) calibration, yielding ~4 kbar for amphibole cores (amphibole rim compositions were not suitable for the Al-in-hornblende calibrations, because of their high silica content, higher than 50 wt %; Table 2b). However, Al-in-hornblende geobarometers tend to overestimate pressures, as both the pressure-dependent tschermakitic and the temperature-dependent edenitic substitutions govern the total Al content in amphiboles (Erdmann *et al.* 2014).

Pressures range from 2.15 to 3.36 kbar when calculated with the geobarometer of Molina *et al.* (2015) and the temperatures obtained with the pressure-independent thermometer B2 from Molina *et al.* (2021).

Similar pressures were obtained using the Molina *et al.* (2015) geobarometer combined with the temperatures obtained with the Ridolfi & Renzulli (2012) and Putirka (2016) thermometers (Table 4). These pressures broadly agree with the ones obtained with the Anderson & Smith (1995) amphibole barometer (2.26–3.13; Table 4).

5.b.2. Oxygen fugacity

The oxygen fugacity of the parental melt to the Varvarco Tonalite was calculated using the method of Ridolfi *et al.* (2010) and Wones & Eugster (1965) (Fig. 18a, d). Ridolfi *et al.* (2010) uses amphibole AQ18 chemistry to derive pressure–temperature (P–T) conditions, H_2O and fO_2. It should be noted that the Ridolfi *et al.* (2010) barometer estimates pressures of ~1.1 kbar for amphibole cores and 0.7 kbar for rims, which is significantly lower than pressures derived with other barometers. However, pressure differences within 1–3 kbar have very little effect (~0.2 log unit) on the fO_2 estimates by the Ridolfi *et al.* (2010) oxybarometer, which is within the uncertainty of the method (0.4 log unit). According to the Ridolfi *et al.* (2010) oxybarometer, amphibole cores and rims from the Varvarco Tonalite have similar oxygen fugacities in the range of −12.2–14.9 logfO_2, which indicates that they crystallized under relatively high fO_2 conditions between the nickel–nickel oxide (NNO) and NNO + 2 buffers, typical of calc-alkaline magmas (ΔNNO from −1 to +3; e.g. Gill, 1981; Behrens & Gaillard, 2006).

Wones & Eugster (1965) used Mg/(Mg + Fe) ratios in biotite and temperatures in order to estimate fO_2. We used temperatures derived by Henry *et al.* (2005) and biotite cations by Li *et al.* (2020). All biotites plot in the area outlined by a yellow circle (Fig. 18d). For comparison, biotites by Castro *et al.* (2011) plot over the wider ranges of fO_2, but still between the NNO and haematite–magnetite (HM) buffers.

Oxygen fugacities between the NNO and HM buffers are also suggested by the Fe^{2+}–Fe^{3+}–Mg ternary diagram for biotite compositions of Wones & Eugster (1965) (Fig. 18c). Additionally, high oxygen fugacities of the studied rocks are also inferred from the $Fe_t/(Fe_t + Mg)$ ratios in amphibole (Czamanske & Wones, 1973; Anderson & Smith, 1995), and by titanomagnetite as the main oxide phase of these rocks (see below, Fig. 18b; online Supplementary Material Fig. S2a).

5.c. Cooling history and exhumation of the Late Cretaceous and Palaeogene plutons

To date, three ages have been obtained for the Varvarco Tonalite: a recalculated K–Ar biotite age of 64.7 ± 3.2 Ma (J.I.C.A./M.M.A.J., 2000 *in* Franchini *et al.* 2003), an ^{40}Ar–^{39}Ar biotite age of 69.09 ± 0.13 Ma (Kay *et al.* 2006) and recently a U–Pb SHRIMP zircon age of 67.8 ± 0.8 Ma (Assis, 2019). Zappettini *et al.* (2014) and Zappettini *et al.* (2021) reported an ^{40}Ar–^{39}Ar age of 65.68 ± 0.22 Ma for adularia from veins associated with the hydrothermal alteration of basic volcanic rocks from the Jurassic Colomichicó Formation (Zappettini *et al.* 2018).

If the closure temperatures of the specific minerals for the various geochronological methods are taken into account, it is possible to construct a thermal profile and to calculate the exhumation rate

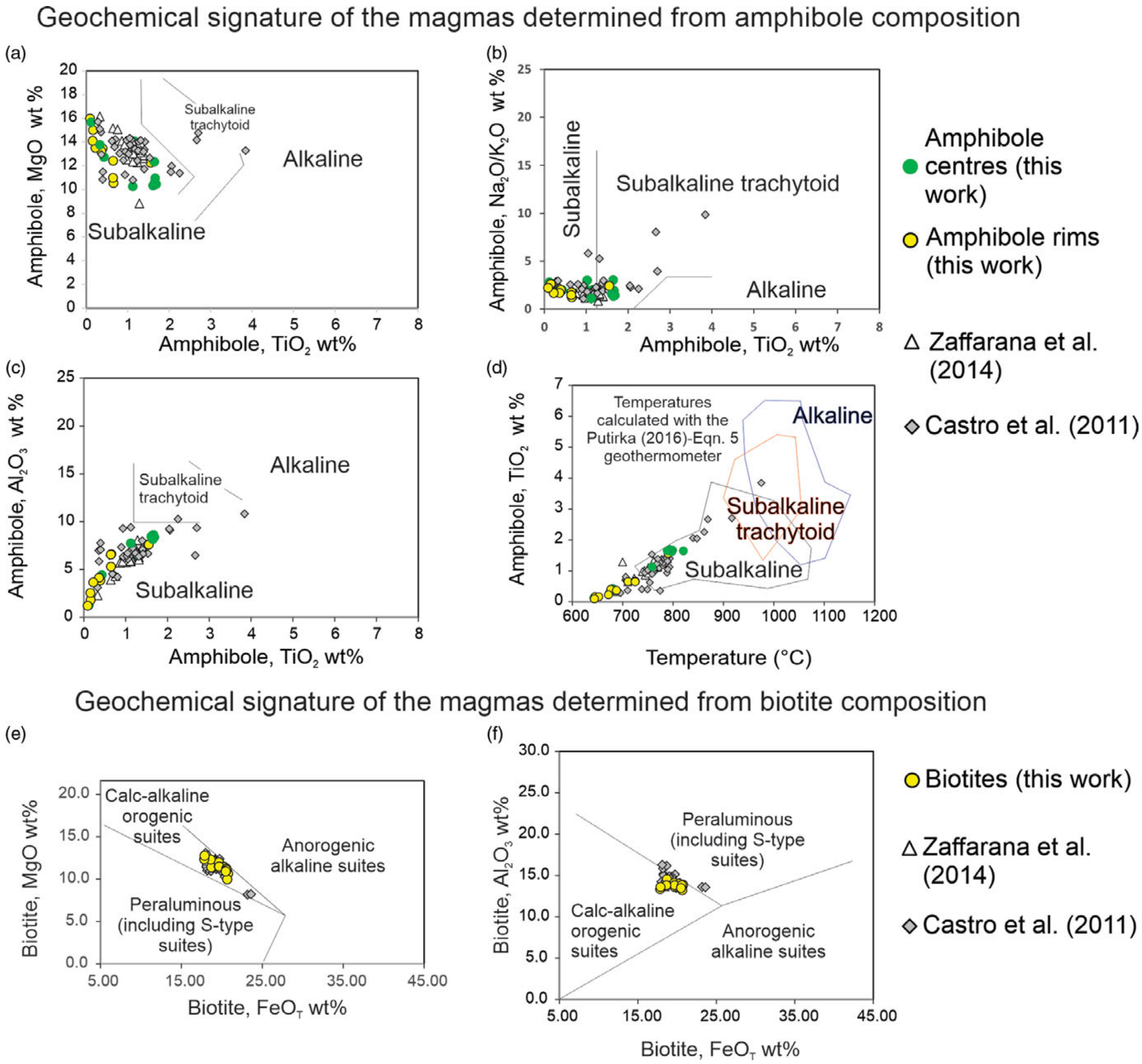

Fig. 17. (Colour online) Geochemical signature of the magmas in equilibrium with amphibole and biotite from the Varvarco Tonalite. (a–d) Amphibole compositions of the Varvarco Tonalite plotted on the diagrams of Molina *et al*. (2009). (a) MgO versus TiO_2. (b) Na_2O/K_2O versus TiO_2. (c) Al_2O_3 versus TiO_2. (d) TiO_2 versus temperature calculated AQ19 using geothermometer of Putirka (2016). (e, f) Tectonic discrimination diagrams for biotites of the Varvarco Tonalite: (e) MgO versus FeO_T and (f) Al_2O_3 versus FeO_T (Abdel-Rahman, 1994).

(England & Molnar, 1990). Thus, the thermal profile/cooling curve for the Varvarco Tonalite was constructed (Fig. 19) considering the more accurate geochronological data, namely those obtained by Assis (2019) and Zappettini *et al*. (2014). The typical closure temperature for U–Pb on zircon is greater than 800 ° C (Lee *et al*. 1997). Siégel *et al*. (2018) showed that the zircon saturation temperature in igneous rocks is variable, but normally between 780 and 860 °C for intrusive rocks. Since we do not have Ti-in-zircon data that would allow us to calculate temperatures more precisely, we assume a closure temperature for zircon of *c*. 850 °C. Considering that the closure temperature of radiogenic argon in K-feldspar can be as low as 120–150 °C (Foland, 1974; Harrisson & McDougall, 1982), we opted for using a closure temperature of 150 °C for adularia.

A one-step theoretical curve between 67.8 ± 0.8 Ma (U–Pb in zircon) and 65.68 ± 0.22 Ma (^{40}Ar–^{39}Ar in adularia from hydrothermal veins) was constructed for the exhumation of the Varvarco Tonalite (Fig. 19). This curve gives a continuous cooling rate of ~330 °C per Ma. Sánchez *et al*. (2018) proposed tectonically driven continuous exhumation for the Cordillera del Viento during the latest Cretaceous – early Palaeogene deformation event. Considering continuous and fast exhumation, the theoretical curve can be extended below 100 °C towards the graphically obtained age of 65.3 Ma (Fig. 19). Fast cooling and exhumation of the Varvarco Tonalite also agrees with the low pressures obtained by geothermobarometry (Tables 2, 4). The highest pressures calculated for amphibole and plagioclase cores are of the order of 3.37 kbar, which correspond to a source at ~12 km depth. Amphibole rims

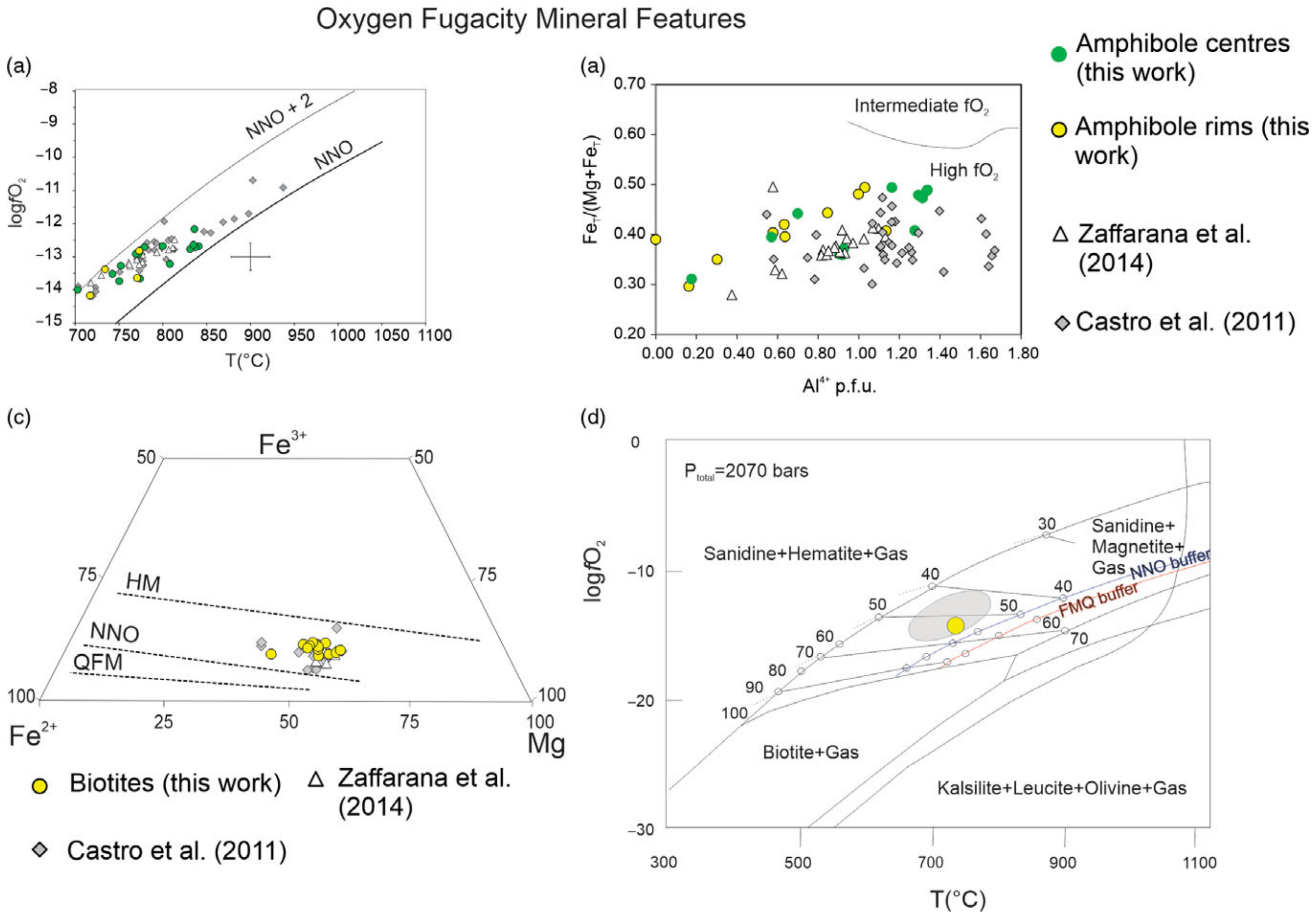

Fig. 18. (Colour online) Oxygen fugacity conditions of the magmas in equilibrium with the amphiboles and biotites of the Varvarco Tonalite. Data from Zaffarana *et al*. (2014) and Castro *et al*. (2011) are plotted for comparison. (a) logfO_2 versus temperature diagram of Ridolfi *et al*. (2010). Error bars represent maximum logfO_2 errors of 0.4 log unit and the expected σ (22 °C). (b) Diagram of Anderson & Smith (1995) showing the effect of fO_2 on amphibole compositions in terms of $Fe_T/(Fe_T + Mg)$ versus Al^{IV} (apfu). (c) Ternary diagram for oxygen fugacity in biotites (Wones & Eugster, 1965). (d) logfO_2 versus *T* diagram (Wones & Eugster, 1965). Numbers represent 100*Mg/(Mg + Fe) ratios in biotites. Yellow circle shows an average of all biotite compositions from this study. Biotites from Zaffarana *et al*. (2014) overlap with the yellow circle. Biotites from Castro *et al*. (2011) are shown in the grey oval. Oxygen fugacity buffers are nickel–nickel oxide (NNO), haematite–magnetite (HM) and quartz–fayalite–magnetite (FMQ).

crystallized at lower pressures of ~1–2 kbar, which is compatible with shallower emplacement at ~4–7 km depth. It means that if the exhumation was a continuous process, as suggested by the thermal profile, the magmatic system could have been exhumed by ~12 km in *c*. 2.1 Ma.

Considering that the Palaeogene Cayanta Volcanics intruded over the already eroded Varvarco Tonalite and Radales Aplite between 50–56.9 Ma (^{40}Ar–^{39}Ar hornblende ages, Jordan *et al.* 2001) and 67.5 ± 8 Ma (AFT age), and the Varvarco Tonalite has a final stage of exhumation (below 4–5 km) at least at 59.5 Ma, one important question that we are trying to answer is 'When was the final exhumation of the Varvarco Tonalite plus Radales Aplite?' The final tectonic exhumation must have occurred after the crystallization of the adularia veins in the Radales Aplite at 65.68 ± 0.22 Ma and prior to the extrusion of the Cayanta volcanic rocks at 56.9–50 Ma. The Varvarco Tonalite magmatic fabric was not affected by any solid-state deformation that could have been superimposed onto these rocks, and shallow emplacement conditions helped in the fast exhumation process. The Radales Aplite has a granophyric texture, which suggests that it would have experienced a greater degree of undercooling than the Varvarco Tonalite (Vernon, 2010), consistent with emplacement at a shallower crustal level. At this point, we do not have any crystallization age for the Radales Aplite that may corroborate the relationship between cooling and exhumation. The final exhumation possibly occurred coevally with the generation of the adularia veins in the Radales Aplite at 65.68 Ma or later as part of the continuous process of exhumation at 65.3 Ma (Fig. 19), or between 65.3 and 59.5 Ma, considering the AFT age. We do not exclude that the final exhumation could have happened after 59.5 Ma, but certainly before 56.9 Ma.

Note that the K–Ar biotite cooling age of 64.7 ± 3.2 Ma (Franchini *et al.* 2003) falls onto this cooling curve given the uncertainty of the fission-track ages. The biotite age of 69.09 ± 0.13 Ma, also from the Varvarco Tonalite (Kay *et al.* 2006), is much older than the U–Pb zircon age of Assis (2019). These two ages are not within the uncertainty. It is difficult to explain this age difference in the context of the thermal profile, but it could be related to an early (*c*. 69 Ma) input of mafic hydrated magma into the magmatic system of the Varvarco Tonalite.

Given the age of 50.3 ± 5.9 Ma (AFT, sample BU4), the Butalón Tonalite was exhumed a little later than the Varvarco Tonalite, in Palaeogene time. However, the exact age of its exhumation is not yet fully constrained. The AFT age of the Butalón Tonalite is not as well defined as that for the Varvarco Tonalite, because less fission-track data could be obtained from the dated sample BU4 (Table 3).

Table 4. Summary of the temperatures and pressures calculated for the sample of the Varvarco Tonalite

Calibration	Sample name / Analysed material		Calibration uncertainty	Varvarco Tonalite Centres	Rims
	Amp-Pl thermometer (Molina *et al.* 2021 –expression A1 at 5 kbar)		± 50 °C	**623**–691	–
	Amp-Pl thermometer (Molina *et al.* 2021 –expression A1 at 1 kbar)		± 50 °C	624–692	–
	Amp-Pl thermometer (Molina *et al.* 2021 –expression A2 at 5 kbar)		± 50 °C	636–699	–
	Amp-Pl thermometer (Molina *et al.* 2021 –expression A2 at 1 kbar)		± 50 °C	637–699	–
	Amp-Pl thermometer (Molina *et al.* 2021 –expression B2)		± 50 °C	641–**703**	–
	Amp-Pl thermometer (Holland & Blundy, 1994 –expression B)		± 40 °C	784–716	–
	Amphibole data (available in Table 2b)	Amp-only thermometer of Ridolfi *et al.* (2010) – Eqn. 1. Average data	± 35 °C	780	742
		Amp-only thermometer of Ridolfi & Renzulli (2012) – Eqn. 2. Average data	± 32 °C	717	614
		Amp-only thermometer of Putirka (2016) – Eqn. 5. Average data.	± 30 °C	742	678
	Whole-rock data (calculated with sample BPN11 of Varvarco Tonalite from Kay *et al.* 2006)	Liquid-only – Molina *et al.* (2015)	± 35 to ± 45 °C	958	
		Liquid-only – Putirka (2016) – Eqn.3	± 33 °C	922	
	Biotite (available in Table 2c)	Henry *et al.* (2005)	± 12 °C	689–753	
Geobarometers (kbar)	Amphibole data (some of them are available in Table 2b)	Hammarstrom & Zen (1986) (average data)	± 3 kbar	3.47	–
		Hollister *et al.* (1987) (average data)	± 1 kbar	3.53	–
		Johnson & Rutherford (1989) (average data)	± 0.5 kbar	2.76	–
		Schmidt (1992) (average data)	± 0.6 kbar	3.99	–
		Ridolfi & Renzulli (2012) – Average between Eqn. 1a and Eqn. 1b	± 2.5 kbar	1.20	0.7
	Amp-Pl barometer (Anderson & Smith, 1995)		± 0.6 kbar	3.13–2.26	–
	Amp–Pl barometer (Molina *et al.* 2015) at T1*		± 1.5 to ± 2.3 kbar	3.37–2.28	–
	Amp–Pl barometer (Molina *et al.* 2015) at T2**			2.64–1.83	–
	Amp–Pl barometer (Molina *et al.* 2015) at T3***			3.36–2.15	–

AQ20 In the amphibole–plagioclase barometer of Molina *et al.* (2015), T1 is the temperature obtained with the Ridolfi & Renzulli (2012) geothermometer (equation 2) and T2 with the Putirka (2016) geothermometer (equation 5). Standard deviation of the data is signalled in the appropriate cases. Errors are 1 sigma standard deviations.
T1* (Ridolfi & Renzulli, 2012, Eqn. 2)
T2** (Putirka, 2016, Eqn. 5)
T3*** (Molina *et al.* 2021, expression B2)

It seems that the Butalón Tonalite was emplaced in an already exhumed orogenic system. This is also in agreement with the different cooling rates of the Varvarco Tonalite and the Radales Aplite, as inferred from their magmatic textures discussed before.

Temperature and pressure estimates derived from mineral chemistry are here integrated with the temperature–time path reconstruction in order to derive a geothermal gradient for the Cordillera del Viento area. In the first place, amphibole core compositions provide temperatures of ~620–700 °C and pressures of ~2–3.36 kbar, which correspond to nearly ~12 km depth (Fig. 19). At these *P*–*T* conditions, the Varvarco Tonalite was almost completely crystallized and already cooling. Then, amphibole rim compositions record pressures of 1–2 kbar, which correspond to ~4–7 km depth (Fig. 19), and, at this stage, the temperatures were no higher than 120 °C, as apatite fission tracks anneal at temperatures higher than this threshold (Ehlers & Farley, 2003; Reiners & Ehlers, 2005). From these two *T* and *P* regimes, a geothermal gradient of ~62.5 °C km^{-1} can be obtained, revealing the cooling and exhumation history of the Varvarco Tonalite. Such a high geothermal gradient suggests that the intrusive rocks were cooling down and exhuming at the same time. The lower geothermal gradients of ~51 °C km^{-1} (Sigismondi, 2013; Sigismondi & Ramos, 2009*a*,*b*; see Galetto *et al.* 2021) could be reflecting the pre-Andean tectonic scenario in the modern easternmost region of the Neuquén Basin, which was not affected by Andean deformation (Galetto *et al.* 2021).

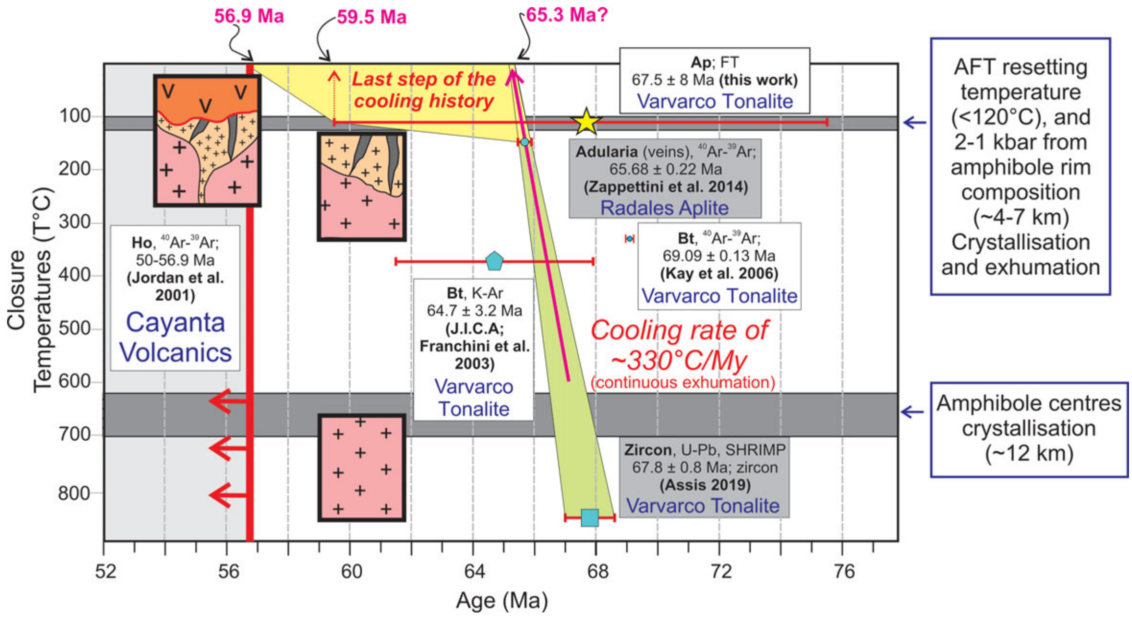

Fig. 19. (Colour online) Cooling history of the Varvarco Tonalite. See main text for details.

5.d. Magnetic fabrics of magmatic origin in the Late Cretaceous and Palaeogene plutons

As previously shown in Section 4.d, the magnetic fabrics determined by the ASM method in the Varvarco Tonalite, Butalón Tonalite and Radales Aplite can be interpreted as being of pure magmatic origin representative of magma flow during Late Cretaceous–Palaeogene times. In particular, the fast-cooling rate estimated from the U–Pb, $^{40}Ar–^{39}Ar$ and AFT ages suggests that the magmatic fabrics of the Varvarco Tonalite were acquired during pluton cooling and exhumation.

The magmatic fabrics from the Varvarco Tonalite and Radales Aplite are steeply dipping, with a predominant N–S strike (online Supplementary Material Fig. S1a), which is mostly consistent with the orientation of the regional structures from the Andean orogenic cycles (Giacosa *et al.* 2014; Turienzo *et al.* 2018; Sánchez *et al.* 2018). The oscillating character of the magmatic fabrics strongly suggests that they could have been influenced by intrinsic dynamics inside the magma chamber. However, there is some evidence of regional stress influence, such as N–S elongation of the pluton along the Matancillas creek (Figs 2a, 3a, b) and NNE–SSW to NNW–SSE fabrics. Even though coupling with the wall rock may not occur, the Andean stress field might have influenced magma flow to some extent. The N–S Matancillas creek goes along the trace of the N–S-directed Cordillera del Viento Fault (Fig. 2a, b). This fault was active during the Andean deformation and could have favoured magma ascent through the crust. The lack of tectonic deformation suggests that pluton emplacement took place either during or soon after the Late Cretaceous deformation event in the Neuquén Andes. Alternatively, similar fabrics may be possible even during a regional deformation event if strain partitioning in low- versus high-strain domains is present. However, post-tectonic emplacement is also in agreement with observations made in the other parts of the Naunauco Belt, where other subvolcanic bodies were post-tectonically emplaced (Llambías & Malvicini, 1978; Zamora Valcarce *et al.* 2011).

Other plutons that were emplaced late with respect to the main tectonic deformation events have been described as having flat roofs and steeply dipping foliation planes along the pluton walls (de Saint-Blanquat *et al.* 2006; Payacán *et al.* 2014). Their internal fabric is strongly decoupled from the host rock fabrics, likely reflecting magma chamber processes (Paterson *et al.* 1998).

Unfortunately, the areas of the Varvarco Tonalite (marked as 'VT' in Fig. 2 and Fig. 3a, b) where we expected to see flattened magmatic foliations in the roof of the intrusion, were only inferred from satellite images and inaccessible for sampling. Some sites, such as site V3, within the Varvarco Tonalite show flat foliation planes, suggesting a location near the pluton roof. But in general, steeply dipping magmatic foliations are dominant and probably reflect closeness to the contact with the host rocks. The contact area is the place where the highest degree of coupling between the magmatic and host rock fabrics usually occurs (Paterson *et al.* 1998). In this sense, the parallel foliations presented by the metamorphic rocks of the Guaracó Norte Formation and the magmatic rocks of the Varvarco and Radales plutons in the area between the Matancilla and Chacay creeks suggest that some degree of mechanical coupling existed between them (Fig. 12a). However, the contact aureole in the margin-parallel fabrics rules out regional deformation as a significant cause of fabric formation, and instead suggests late fabric formation due to internal processes during emplacement (Paterson *et al.* 1998). In addition, the thermal contrast between the Guaracó Norte Formation and the Varvarco Tonalite is consistent with the results obtained from geothermobarometry, which suggests that the Varvarco pluton was emplaced at a high crustal level at ~2–3 kbar (between 7 and 11 km depth).

Lastly, magma feeder zones, where magma upwelled, can be traced by the existence of vertical magmatic lineations at sites for which AMS ellipsoids of prolate shape ($T < 0$) were measured, such as V1, V2, V6 and V7 from the Varvarco Tonalite (online Supplementary Material Fig. S1f). **AQ21**

6. Conclusions

Field observations and petrographic analysis indicate that magma hybridization was the main process in the Varvarco and Butalón plutons. The magnetic fabrics of these plutons are dominated by titanomagnetite. This, together with the mineral chemistry data (amphibole and biotite) confirms that these magmatic phases belong to the I-type series of calc-alkaline igneous bodies.

The fabrics are, without exception, magmatic, and the AMS data can be interpreted as the result of emplacement and rapid exhumation of fast-cooled plutons. The AFT ages of the Varvarco Tonalite are close to its crystallization age, as well as the fast-cooling age calculated for this pluton (330 °C Ma^{-1}; Fig. 19). Shallow emplacement conditions were estimated based on geothermobarometry (2–3 kbar, equivalent to 12 km depth). These combined data allow us to infer uplift in the region between 66 and 64.9 Ma. Geothermobarometry and AFT data suggest a geothermal gradient for the area of ~62.5 °C km^{-1}. The magmatic system in the Varvarco area could have been exhumed by ~12 km in *c.* 2.1 Ma.

The orientation of the magmatic fabrics implies that they formed mostly owing to magma chamber processes. However, they could have been controlled, in part, by the regional Late Cretaceous compressive deformation. As the plutons are located along the trace of the Cordillera del Viento Fault, and because they are devoid of post-emplacement tectonic deformation, reactivations of this fault are not supported.

Acknowledgements. We want to thank Dr Sebastián Oriolo and an anonymous reviewer for their valuable suggestions that greatly improved the manuscript. We cordially thank Fuat Yavuz for help with biotite diagrams in the earlier version of this article. The research projects from the Universidad Nacional de Río Negro (UNRN) PI-40-A-466, PI-40-A-547, PI-40-A-631, PI-40-A-798 and PI-40-A-916; project PIP CONICET 2015-2017 11220150100736CO; PICT 2019-01809; project CGL 2012-38396-C01 of the Spanish Programme for Science Technology (I+D+i) and FEDER Funds of the EU, contributed to finance this work. The research of José F. Molina has been supported for the Ministerio de Economía y Competitividad (Gobierno de España), grant numbers: CGL2013-40785-P and CGL2017-84469-P, and Consejería de Economía y Conocimiento (Junta de Andalucía), grant number: RNM2163. The research of Natalia Hauser has been supported in part by CNPq fellowships (grants 309878/2019-5). This study was financed in part by the Coordenação de Aperfeiçoamento de Pessoal de Nivel Superior – Brasil (CAPES) – Finance Code 001.

Supplementary material. To view supplementary material for this article, please visit https://doi.org/10.1017/S0016756821001163

References

Abdel-Rahman A-FM (1994) Nature of biotites from alkaline, calc-alkaline, and peraluminous magmas. *Journal of Petrology* **35**, 525–41. doi: 10.1093/petrology/35.2.525

Allmendinger RW, Cardozo N and Fisher DM (2012) *Structural Geology Algorithms: Vectors and Tensors*. Cambridge: Cambridge University Press, 289 pp. doi: 10.1017/CBO9780511920202

Anderson JL and Smith DR (1995) The effects of temperature and fO_2 on the Al-in-hornblende barometer. *American Mineralogist* **80**, 549–59. doi: 10.2138/am-1995-5-614

Archanjo CJ, Launeau P and Bouchez JL (1995) Magnetic fabric vs. magnetite and biotite shape fabrics of the magnetite-bearing granite pluton of Gameleiras (Northeast Brazil). *Physics of the Earth and Planetary Interiors* **89**, 63–75. doi: 10.1016/0031-9201(94)02997-P

Archanjo CJ, Trindade RIF, Bouchez JL and Ernesto M (2002) Granite fabrics and regional-scale strain partitioning in the Seridó belt (Borborema Province, NE Brazil). *Tectonics* **21**, 1003. doi: 10.1029/2000TC001269

Arregui C, Carbone O and Leanza HA (2011) Contexto tectosedimentario. In *Relatorio Del 18° Congreso Geológico Argentino, Neuquén*, pp. 29–36.

Assis OS (2019) *Petrografía y fábrica magnética de la Granodiorita Varvarco y plutones asociados, Cretácico Tardío-Paleoceno de los Andes Neuquinos*. Final degree project in geology, Universidad Nacional de Río Negro, Argentina. Published thesis http://rid.unrn.edu.ar/jspui/handle/20.500.12049/2256 **AQ22**

Bachmann O and Bergantz GW (2008) Deciphering magma chamber dynamics from styles of compositional zoning in large silicic ash flow sheets. *Reviews in Mineralogy and Geochemistry* **69**, 651–74. doi: 10.2138/rmg.2008.69.17

Barbarin B (2005) Mafic magmatic enclaves and mafic rocks associated with some granitoids of the central Sierra Nevada batholith, California: nature, origin, and relations with the hosts. *Lithos* **80**, 155–77. doi: 10.1016/j.lithos.2004.05.010

Bateman R (1995) The interplay between crystallization, replenishment and hybridization in large felsic magma chambers. *Earth-Science Reviews* **39**, 91–106. doi: 10.1016/0012-8252(95)00003-S

Bateman PC and Eaton JP (1967) Sierra Nevada Batholith. *Science* **158**, 1407–17.

Baxter S and Feely M (2002) Magma mixing and mingling textures in granitoids: examples from the Galway Granite, Connemara, Ireland. *Mineralogy and Petrology* **76**, 63–74. doi: 10.1007/s007100200032 **AQ23**

Behrens H and Gaillard F (2006) Geochemical aspects of melts: volatiles and redox behavior. *Elements* **2**, 275–80. doi: 10.2113/gselements.2.5.275

Borradaile GJ and Henry B (1997) Tectonic applications of magnetic susceptibility and its anisotropy. *Earth-Science Reviews* **42**, 49–93. doi: 10.1016/S0012-8252(96)00044-X

Borradaile GJ and Jackson M (2010) Structural geology, petrofabrics and magnetic fabrics (AMS, AARM, AIRM). *Journal of Structural Geology* **32**, 1519–51. doi: 10.1016/j.jsg.2009.09.006

Bouchez J-L (2000) Anisotropie de susceptibilité magnétique et fabrique des granites. *Comptes Rendus de l'Académie des Sciences, Series IIA, Earth and Planetary Science* **330**, 1–14. doi: 10.1016/S1251-8050(00)00120-8

Cardozo N and Allmendinger RW (2013) Spherical projections with OSXStereonet. *Computers & Geosciences* **51**, 193–205. doi: 10.1016/j.cageo.2012.07.021

Casé AM, López-Escobar L, Danieli JC and Schalamuk A (2008) Butalón igneous rocks, Neuquén, Argentina: age, stratigraphic relationships and geochemical features. *Journal of South American Earth Sciences* **26**, 188–203. doi: 10.1016/j.jsames.2007.11.001

Castro A, Moreno-Ventas I and de la Rosa JD (1991) Multistage crystallization of tonalitic enclaves in granitoid rocks (Hercynian belt, Spain): implications for magma mixing. *Geologische Rundschau* **80**, 109–20. doi: 10.1007/BF01828770

Castro A, Moreno-Ventas I, Fernández C, Vujovich G, Gallastegui G, Heredia N, Martino RDD, Becchio R, Corretgé LGG, Díaz-Alvarado J, Such P, García-Arias M and Liu D-Y (2011) Petrology and SHRIMP U–Pb zircon geochronology of Cordilleran granitoids of the Bariloche area, Argentina. *Journal of South American Earth Sciences* **32**, 508–30. doi: 10.1016/j.jsames.2011.03.011

Chadima M and Jelinek V (2009) Anisoft 4.2: Anisotropy Data Browser for Windows. Brno: Advanced Geoscience Instruments Company (AGICO).

Clark RN (1999) Spectroscopy of rocks and minerals and principles of spectroscopy. In *Manual of Remote Sensing, Volume 3, Remote Sensing for the Earth Sciences* (ed. AN Rencz), pp. 3–58. New York: John Wiley & Sons.

Cobbold PR and Rossello EA (2003) Aptian to recent compressional deformation, foothills of the Neuquén Basin, Argentina. *Marine and Petroleum Geology* **20**, 429–43. doi: 10.1016/S0264-8172(03)00077-1

Czamanske GK and Wones DR (1973) Oxidation during magmatic differentiation, Finnmarka Complex, Oslo Area, Norway: Part 2, the mafic silicates. *Journal of Petrology* **14**, 349–80. doi: 10.1093/petrology/14.3.349

Dale J, Powell R, White RW, Elmer FL and Holland TJB (2005) A thermodynamic model for Ca–Na clinoamphiboles in Na_2O–CaO–FeO–MgO–Al_2O_3–SiO_2–H_2O–O for petrological calculations. *Journal of Metamorphic Geology* **23**, 771–91. doi: 10.1111/j.1525-1314.2005.00609.x

Day R, Fuller M and Schmidt VA (1977) Hysteresis properties of titanomagnetites: grain-size and compositional dependence. *Physics of the Earth and Planetary Interiors* **13**, 260–7.

D'Eramo F, Pinotti L, Tubía JM, Vegas N, Aranguren A, Tejero R and Gómez D (2006) Coalescence of lateral spreading magma ascending through dykes: a mechanism to form a granite canopy (El Hongo pluton, Sierras

Pampeanas, Argentina). *Journal of the Geological Society, London* **163**, 881–92. doi: 10.1144/0016-764905-060

de Saint-Blanquat M, Habert G, Horsman E, Morgan SS, Tikoff B, Launeau P and Gleizes G (2006) Mechanisms and duration of non-tectonically assisted magma emplacement in the upper crust: the Black Mesa pluton, Henry Mountains, Utah. *Tectonophysics* **428**, 1–31. doi: 10.1016/j.tecto.2006.07.014

de Saint Blanquat M and Tikoff B (1997) Development of magmatic to solid-state fabrics during syntectonic emplacement of the Mono Creek Granite, Sierra Nevada Batholith. In *Granite: From Segregation of Melt to Emplacement Fabrics* (ed. JL Bouchez), pp. 231–52. Dordrecht: Springer. doi: 10.1007/978-94-017-1717-5_15

Deer WA, Howie RA and Zussman J (2013) An Introduction to the Rock-Forming Minerals. London: Mineralogical Society of Great Britain and Ireland.

Digregorio JH (1972) Neuquén. In *Geología Regional Argentina* (ed. AF Leanza), pp. 439–505. Córdoba: Academia Nacional de Ciencias.

Digregorio JH and Uliana MA (1980) Cuenca Neuquina. In *Geología Regional Argentina* (ed. JCM Turner), pp. 985–1032. Córdoba: Academia Nacional de Ciencias.

Dunkl I (2002) Trackkey: a Windows program for calculation and graphical presentation of fission track data. *Computers & Geosciences* **28**, 3–12. doi: 10.1016/S0098-3004(01)00024-3

Ehlers TA and Farley KA (2003) Apatite (U–Th)/He thermochronometry: methods and applications to problems in tectonics and surface processes. *Earth and Planetary Science Letters* **206**, 1–14.

England P and Molnar P (1990) Surface uplift, uplift of rocks, and exhumation of rocks. *Geology* **18**, 1173–7. doi: 10.1130/0091-7613(1990)018<1173:SUUORA>2.3.CO;2

Erdmann S, Martel C, Pichavant M and Kushnir A (2014) Amphibole as an archivist of magmatic crystallization conditions: problems, potential, and implications for inferring magma storage prior to the paroxysmal 2010 eruption of Mount Merapi, Indonesia. *Contributions to Mineralogy and Petrology* **167**, 1016. doi: 10.1007/s00410-014-1016-4

Ferré EC and Améglio L (2000) Preserved magnetic fabrics vs. annealed microstructures in the syntectonic recrystallised George granite, South Africa. *Journal of Structural Geology* **22**, 1199–219. doi: 10.1016/S0191-8141(00)00026-2

Foland KA (1974) Ar^{40} diffusion in homogeneous orthoclase and an interpretation of Ar diffusion in K-feldspars. *Geochimica et Cosmochimica Acta* **38**, 151–66.

Foster MD (1960) Interpretation of the composition of trioctahedral micas. *United States Geological Survey Professional Paper* **354**, 11–48.

Franchini M, López-Escobar L, Schalamuk IBA and Meinert L (2003) Magmatic characteristics of the Paleocene Cerro Nevazón region and other Late Cretaceous to Early Tertiary calc-alkaline subvolcanic to plutonic units in the Neuquén Andes, Argentina. *Journal of South American Earth Sciences* **16**, 399–421. doi: 10.1016/S0895-9811(03)00103-2

Galbraith RF (1981) On statistical models for fission track counts. *Journal of the International Association for Mathematical Geology* **13**, 471–8. doi: 10.1007/BF01034498

Galetto A, Georgieva V, García VH, Zattin M, Sobel ER, Glodny J, Bordese S, Arzadún G, Bechis F, Caselli AT and Becchio R (2021) Cretaceous and Eocene rapid cooling phases in the Southern Andes (36°–37°S): insights from low-temperature thermochronology, U–Pb geochronology and inverse thermal modeling from Domuyo area, Argentina. *Tectonics* **40**, 1–30. doi: 10.1029/2020TC006415

Giacosa R, Allard J, Foix N and Heredia N (2014) Stratigraphy, structure and geodynamic evolution of the Paleozoic rocks in the Cordillera del Viento (37° S latitude, Andes of Neuquén, Argentina). *Journal of Iberian Geology* **40**, 331–48. doi: 10.5209/rev_JIGE.2014.v40.n2.45301

Gill JB (1981) *Orogenic Andesites and Plate Tectonics*. Berlin, Heidelberg: Springer-Verlag. doi: 10.1007/978-3-642-68012-0

Green PF (1981) A new look at statistics in fission-track dating. *Nuclear Tracks* **5**, 77–86. doi: 10.1016/0191-278X(81)90029-9

Grégoire V, de Saint Blanquat M, Nédélec A and Bouchez J-L (1995) Shape anisotropy versus magnetic interactions of magnetite grains: experiments and application to AMS in granitic rocks. *Geophysical Research Letters* **22**, 2765–8. doi: 10.1029/95GL02797

Gulisano CA, Gutiérrez Pleimling AR and Digregorio RE (1984) Esquema estratigráfico de la secuencia jurásica del oeste de la provincia del Neuquén. In *9° Congreso Geológico Argentino*, pp. 236–59.

Hammarstrom JM and Zen E (1986) Aluminum in hornblende: an empirical igneous geobarometer. *American Mineralogist* **71**, 1297–313.

Harrison TM and McDougall I (1982) The thermal significance of potassium feldspar K–Ar ages inferred from ^{40}Ar/^{39}Ar age spectrum results. *Geochimica et Cosmochimica Acta* **46**, 1811–20.

Henry DJ, Guidotti CV and Thomson JA (2005) The Ti-saturation surface for low-to-medium pressure metapelitic biotites: implications for geothermometry and Ti-substitution mechanisms. *American Mineralogist* **90**, 316–28.

Hervé F, Pankhurst RJ, Fanning CM, Calderón M and Yaxley GM (2007) The South Patagonian batholith: 150 my of granite magmatism on a plate margin. *Lithos* **97**, 373–94. doi: 10.1016/j.lithos.2007.01.007

Hibbard MJ (1981) The magma mixing origin of mantled feldspars. *Contributions to Mineralogy and Petrology* **76**, 158–70. doi: 10.1007/BF00371956

Hibbard MJ (1991) Textural anatomy of twelve magma-mixed granitoid systems. In *Enclaves and Granite Petrology* (eds J Didier and B Barbarin), pp. 431–44. Amsterdam: Elsevier.

Higgins MD (2011) Textural coarsening in igneous rocks. *International Geology Review* **53**, 354–76. doi: 10.1080/00206814.2010.496177

Higgins MD and Roberge J (2003) Crystal size distribution of plagioclase and amphibole from Soufriere Hills Volcano, Montserrat: evidence for dynamic crystallization-textural coarsening cycles. *Journal of Petrology* **44**, 1401–11. doi: 10.1093/petrology/44.8.1401

Holland T and Blundy J (1994) Non-ideal interactions in calcic amphiboles and their bearing on amphibole-plagioclase thermometry. *Contributions to Mineralogy and Petrology* **116**, 433–47. doi: 10.1007/BF00310910

Hollister LS, Grissom GC, Peters EK, Stowell HH and Sisson VB (1987) Confirmation of the empirical correlation of Al in hornblende with pressure of solidification of calc-alkaline plutons. *American Mineralogist* **72**, 231–9.

Howell JA, Schwarz E, Spalletti LA and Veiga GD (2005) The Neuquén Basin: an overview. In *The Neuquén Basin, Argentina: A Case Study in Sequence Stratigraphy and Basin Dynamics* (eds GD Veiga, LA Spalletti, JA Howell and E Schwarz), pp. 1–14. Geological Society of London, Special Publication no. 252.

Hrouda F (1982) Magnetic anisotropy of rocks and its application in geology and geophysics. *Geophysical Surveys* **5**, 37–82. doi: 10.1007/BF01450244 AQ24

Hurford AJ and Green PF (1982) A users' guide to fission track dating calibration. *Earth and Planetary Science Letters* **59**, 343–54. doi: 10.1016/0012-821X(82)90136-4

Hurford AJ and Green PF (1983) The zeta age calibration of fission-track dating. *Chemical Geology* **41**, 285–317. doi: 10.1016/S0009-2541(83)80026-6

Ishihara S (1977) The magnetite-series and ilmenite-series granitic rocks. *Mining Geology* **27**, 293–305.

Jelínek V (1978) Statistical processing of anisotropy of magnetic susceptibility measured on groups of specimens. *Studia Geophysica et Geodaetica* **22**, 50–62. doi: 10.1007/BF01613632

Jelinek V (1981) Characterization of the magnetic fabric of rocks. *Tectonophysics* **79**, T63–T67. doi: 10.1016/0040-1951(81)90110-4

Johnson MC and Rutherford MJ (1989) Experimental calibration of the aluminum-in-hornblende geobarometer with application to Long Valley caldera (California) volcanic rocks. *Geology* **17**, 837–41. doi: 10.1130/0091-7613(1989)017<0837:ECOTAI>2.3.CO;2

Jordan TE, Burns WM, Veiga R, Pángaro F, Copeland P, Kelley S and Mpodozis C (2001) Extension and basin formation in the southern Andes caused by increased convergence rate: a mid-Cenozoic trigger for the Andes. *Tectonics* **20**, 308–24. doi: 10.1029/1999TC001181

Kawakatsu K and Yamaguchi Y (1987) Successive zoning of amphiboles during progressive oxidation in the Daito-Yokota granitic complex, San-in belt, southwest Japan. *Geochimica et Cosmochimica Acta* **51**, 535–40. doi: 10.1016/0016-7037(87)90067-6

Kay SM, Burns WM, Copeland P and Mancilla O (2006) Upper Cretaceous to Holocene magmatism and evidence for transient Miocene shallowing of the Andean subduction zone under the northern Neuquén Basin. In *Evolution of an Andean Margin: A Tectonic and Magmatic View from the Andes to the Neuquén Basin (35°–39°S Lat)* (eds SM Kay and VA Ramos), pp. 16–90.

Geological Society of America, Special Papers vol. 407. doi: 10.1130/2006.2407(02)

Kiss B, Harangi S, Ntaflos T, Mason PRD and Pál-Molnár E (2014) Amphibole perspective to unravel pre-eruptive processes and conditions in volcanic plumbing systems beneath intermediate arc volcanoes: a case study from Ciomadul volcano (SE Carpathians). *Contributions to Mineralogy and Petrology* **167**, 986. doi: 10.1007/s00410-014-0986-6

Leake BE, Woolley AR, Arps CES, Birch WD, Gilbert MC, Grice JD, Hawthorne FC, Kato A, Kisch HJ, Krivovichev VG, Linthout K, Laird J, Mandarino J, Maresch WV, Nickel EH, Rock NMS, Schumacher JC, Smith DC, Stephenson NCN, Ungaretti L, Whittaker EJW and Youzhi G (1997) Nomenclature of amphiboles; report of the subcommittee on amphiboles of the International Mineralogical Association Commission on New Minerals and Mineral Names. *Mineralogical Magazine* **61**, 295–321. doi: 10.1180/minmag.1997.061.405.13

Leanza HA, Llambías EJ and Carbone O (2005) Unidades estratigráficas limitadas por discordancias en los depocentros de la Cordillera del Viento y la Sierra de Chacaico durante los inicios de la Cuenca Neuquina. In *6º Congreso de Exploración de Hidrocarburos*, p. 13.

Lee JKW, Williams IS and Ellis DJ (1997) Pb, U and Th diffusion in natural zircon. *Nature* **390**, 159–62. doi: 10.1038/36554

Legarreta L and Uliana MA (1991) Jurassic—marine oscillations and geometry of back-arc basin fill, central Argentine Andes. In *Sedimentation, Tectonics and Eustasy: Sea-level Changes at Active Margins* (ed. DIM Macdonald), pp. 429–50. Oxford: Blackwell Publishing Ltd. doi: 10.1002/9781444303896.ch23

Li X, Chi G, Zhou Y, Deng T and Zhang J (2017) Oxygen fugacity of Yanshanian granites in South China and implications for metallogeny. *Ore Geology Reviews* **88**, 690–701.

Li X, Zhang C, Behrens H and Holtz F (2020) Calculating biotite formula from electron microprobe analysis data using a machine learning method based on principal components regression. *Lithos* **356–357**, 105371. doi: 10.1016/j.lithos.2020.105371

Llambías EJ and Aragón E (2011) Volcanismo Paleógeno. In *Relatorio Del 18º Congreso Geológico Argentino, Neuquén*, pp. 265–74.

Llambías EJ, Leanza HA and Carbone O (2007) Evolución tectono-magmática durante el Pérmico al Jurásico temprano en la Cordillera del Viento (37°05′S – 37°15′S): nuevas evidencias geológicas y geoquímicas del inicio de la Cuenca Neuquina. *Revista de la Asociación Geologica Argentina* **62**, 217–35.

Llambías EJ and Malvicini L (1978) Geología, petrología y metalogénesis del área de Colipilli, provincia del Neuquén, República Argentina. *Revista de la Asociación Geológica Argentina* **33**, 257–76.

Llambías EJ and Rapela CW (1989) Las volcanitas de Collipilli, Neuquén (37°S) y su relación con otras unidades paleógenas de la cordillera. *Revista de la Asociación Geológica Argentina* **44**, 224–36.

McNulty BA, Tobisch OT, Cruden AR and Gilder S (2000) Multistage emplacement of the Mount Givens pluton, central Sierra Nevada batholith, California. *Geological Society of America Bulletin* **112**, 119–35. doi: 10.1130/0016-7606(2000)112<119:MEOTMG>2.0.CO;2

Molina JF, Cambeses A, Moreno JA, Morales I, Montero P and Bea F (2021) A reassessment of the amphibole-plagioclase NaSi–CaAl exchange thermometer with applications to igneous and high-grade metamorphic rocks. *American Mineralogist* **106**, 782–800.

Molina JF, Montero P, Bea F and Scarrow JH (2012) Anomalous xenocryst dispersion during tonalite-granodiorite crystal mush hybridization in the mid crust: mineralogical and geochemical evidence from Variscan appinites (Avila Batholith, Central Iberia). *Lithos* **153**, 224–42. doi: 10.1016/j.lithos.2012.03.021

Molina JF, Moreno JA, Castro A, Rodríguez C and Fershtater GB (2015) Calcic amphibole thermobarometry in metamorphic and igneous rocks: new calibrations based on plagioclase/amphibole Al-Si partitioning and amphibole/liquid Mg partitioning. *Lithos* **232**, 286–305. doi: 10.1016/j.lithos.2015.06.027

Molina JF, Scarrow JH, Montero PG and Bea F (2009) High-Ti amphibole as a petrogenetic indicator of magma chemistry: evidence for mildly alkalic-hybrid melts during evolution of Variscan basic–ultrabasic magmatism of Central Iberia. *Contributions to Mineralogy and Petrology* **158**, 69–98. doi: 10.1007/s00410-008-0371-4

Mollo S, Putirka K, Iezzi G, Del Gaudio P and Scarlato P (2011) Plagioclase-melt (dis)equilibrium due to cooling dynamics: implications for thermometry, barometry and hygrometry. *Lithos* **125**, 221–35. doi: 10.1016/j.lithos.2011.02.008

Nachit H, Ibhi A, Abia EH and Ben Ohoud M (2005) Discrimination between primary magmatic biotites, reequilibrated biotites and neoformed biotites. *Comptes Rendus Geoscience* **337**, 1415–20. doi: 10.1016/j.crte.2005.09.002

Nédélec A and Bouchez J-L (2015) *Granites: Petrology, Structure, Geological Setting, and Metallogeny*. Oxford: Oxford University Press.

Neves SP, Araújo AMB, Correia PB and Mariano G (2003) Magnetic fabrics in the Cabanas Granite (NE Brazil): interplay between emplacement and regional fabrics in a dextral transpressive regime. *Journal of Structural Geology* **25**, 441–53. doi: 10.1016/S0191-8141(02)00003-2

Olivier P, Druguet E, Castaño LM and Gleizes G (2016) Granitoid emplacement by multiple sheeting during Variscan dextral transpression: the Saint-Laurent – La Jonquera pluton (Eastern Pyrenees). *Journal of Structural Geology* **82**, 80–92. doi: 10.1016/j.jsg.2015.1b.d.l.6

Pankhurst RJ, Weaver SD, Hervé F and Larrondo P (1999) Mesozoic–Cenozoic evolution of the North Patagonian Batholith in Aysen, southern Chile. *Journal of the Geological Society, London* **156**, 673–94. doi: 10.1144/gsjgs.156.4.0673

Paterson SR, Fowler TK, Schmidt KL, Yoshinobu AS, Yuan ES and Miller RB (1998) Interpreting magmatic fabric patterns in plutons. *Lithos* **44**, 53–82.

Payacán I, Gutiérrez F, Gelman SE, Bachmann O and Parada MA (2014) Comparing magnetic and magmatic fabrics to constrain the magma flow record in La Gloria pluton, central Chile. *Journal of Structural Geology* **69**, 32–46. doi: 10.1016/j.jsg.2014.09.015

Pesce AH (1981) Estratigrafía de las nacientes del río Neuquén y Nahuever, Provincia del Neuquén. In *Actas 8º Congreso Geológico Argentino*, pp. 439–55.

Putirka K (2016) Amphibole thermometers and barometers for igneous systems and some implications for eruption mechanisms of felsic magmas at arc volcanoes. *American Mineralogist* **101**, 841–58. doi: 10.2138/am-2016-5506

Ramos V (1999) Rasgos estructurales del territorio argentino. In *Geología Argentina* (ed. R Caminos), pp. 715–84. Buenos Aires: Instituto de Geología y Recursos Minerales, Servicio Geológico Minero Argentino.

Ramos V, Mosquera A, Folguera A and García Morabito E (2011) Evolución tectónica de los Andes y del Engolfamiento Neuquino adyacente. In *Relatorio Del 18º Congreso Geologico Argentino, Neuquén*, pp. 335–48.

Ramos VA, Niemeyer H, Skarmeta J and Muñoz J (1982) Magmatic evolution of the Austral Patagonian Andes. *Earth-Science Reviews* **18**, 411–31. doi: 10.1016/0012-8252(82)90047-2

Rapela CW and Llambías EJ (1985) La secuencia andesítica terciaria de Andacollo, Neuquén, Argentina. In *4º Congreso Geológico Chileno*, pp. 458–88.

Reiners PW and Ehlers TA (eds) (2005) Low-temperature Thermochronology: Techniques, Interpretations, and Applications. Reviews in Mineralogy and Geochemistry, vol. 58, 620 pp.

Riccardi AC and Stipanicic PN (2002) Fase diastrófica Río Atuel. In *Léxico Estratigráfico de La Argentina. Triásico* (eds PN Stipanicic and CA Marsicano), p. 245. Buenos Aires: Asociación Geológica Argentina.

Ridolfi F, Puerini M, Renzulli A, Menna M and Toulkeridis T (2008) The magmatic feeding system of El Reventador volcano (Sub-Andean zone, Ecuador) constrained by texture, mineralogy and thermobarometry of the 2002 erupted products. *Journal of Volcanology and Geothermal Research* **176**, 94–106. doi: 10.1016/j.jvolgeores.2008.03.003

Ridolfi F and Renzulli A (2012) Calcic amphiboles in calc-alkaline and alkaline magmas: thermobarometric and chemometric empirical equations valid up to 1,130°C and 2.2 GPa. *Contributions to Mineralogy and Petrology* **163**, 877–95. doi: 10.1007/s00410-011-0704-6

Ridolfi F, Renzulli A and Puerini M (2010) Stability and chemical equilibrium of amphibole in calc-alkaline magmas: an overview, new thermobarometric formulations and application to subduction-related volcanoes. *Contributions to Mineralogy and Petrology* **160**, 45–66. doi: 10.1007/s00410-009-0465-7

Rochette P, Aubourg C and Perrin M (1999) Is this magnetic fabric normal? A review and case studies in volcanic formations. *Tectonophysics* **307**, 219–34. doi: 10.1016/S0040-1951(99)00127-4

Rochette P, Jackson M and Aubourg C (1992) Rock magnetism and the interpretation of anisotropy of magnetic susceptibility. *Reviews of Geophysics* **30**, 209. doi: 10.1029/92RG00733

Rovere EI, Caselli A, Tourn S, Leanza HA, Hugo CA, Folguera A, Escosteguy L, Geuna S, González R, Colombino J and Danieli JC (2004) Hoja Geológica 3772-IV, Andacollo, Provincia del Neuquén. Buenos Aires: Instituto de Geología y Recursos Minerales, Servicio Geológico Minero Argentino, Boletín 26. AQ26

Sagripanti L, Folguera A, Giménez M, Rojas Vera EA, Fabiano JJ, Molnar N, Fennell L and Ramos VA (2014) Geometry of Middle to Late Triassic extensional deformation pattern in the Cordillera del Viento (Southern Central Andes): a combined field and geophysical study. *Journal of Iberian Geology* **40**, 349–66. doi: 10.5209/rev_JIGE.2014.v40.n2.45305

Sánchez NP, Coutand I, Turienzo M, Lebinson F, Araujo V and Dimieri L (2018) Tectonic evolution of the Chos Malal Fold-and-Thrust Belt (Neuquén Basin, Argentina) from (U-Th)/He and fission track thermochronometry. *Tectonics* **37**, 1907–29. doi: 10.1029/2018TC004981

Schmidt MW (1992) Amphibole composition in tonalite as a function of pressure: an experimental calibration of the Al-in-hornblende barometer. *Contributions to Mineralogy and Petrology* **110**, 304–10. doi: 10.1007/BF00310745

Siégel C, Bryan SE, Allen CM and Gust DA (2018) Use and abuse of zircon-based thermometers: a critical review and a recommended approach to identify antecrystic zircons. *Earth-Science Reviews* **176**, 87–116. doi: 10.1016/j.earscirev.2017.08.011

Sigismondi ME (2013) *Estudio de la deformacion litosférica de la Cuenca Neuquina: estructura termal, datos de gravedad y sísmica de reflexion*. Ph.D. thesis, Universidad de Buenos Aires, Buenos Aires, Argentina. Published thesis. Biblioteca Digital de la Facultad de Ciencias Exactas y Naturales. http://digital.bl.fcen.uba.ar/Download/Tesis/Tesis_5361_Sigismondi.pdf

Sigismondi M and Ramos VA (2009a) El flujo de calor de la Cuenca Neuquina, Argentina, primera parte. *Revista del Instituto Argentino del Petróleo y Gas, Petrotecnia* **1**, 64–81.

Sigismondi M and Ramos VA (2009b) El flujo de calor de la Cuenca Neuquina, Argentina, segunda parte. *Revista del Instituto Argentino del Petróleo y Gas, Petrotecnia* **2**, 58–76.

Somoza R, Tomlinson AJ, Zaffarana CB, Singer SE, Puigdomenech Negre CG, Raposo MIB and Dilles JH (2015) Tectonic rotations and internal structure of Eocene plutons in Chuquicamata, northern Chile. *Tectonophysics* **654**, 113–30. doi: 10.1016/j.tecto.2015.05.005

Spagnuolo MG, Folguera A, Litvak V, Rojas Vera EA and Ramos VA (2012) Late Cretaceous arc rocks in the Andean retroarc region at 36.5°S: evidence supporting a Late Cretaceous slab shallowing. *Journal of South American Earth Sciences* **38**, 44–56. doi: 10.1016/j.jsames.2012.05.002

Stevenson C (2009) The relationship between forceful and passive emplacement: the interplay between tectonic strain and magma supply in the Rosses Granitic Complex, NW Ireland. *Journal of Structural Geology* **31**, 270–87. doi: 10.1016/j.jsg.2008.11.009

Stipanicic PN (1966) El Jurásico en Vega de la Veranada (Neuquén), el Oxfordense y el diastrofismo Divesiano (Agassiz-Yaila) en Argentina. *Revista de la Asociación Geológica Argentina* **20**, 403–78.

Suárez M and de la Cruz R (1997) Volcanismo pliniano del Lías durante los inicios de la cuenca de Neuquén, Cordillera del Viento, Neuquén, Argentina. *In Actas 7º Congreso Geológico Chileno. Concepción, Vol. 1*, pp. 266–70.

Tischendorf G, Gottesmann B, Förster H-J and Trumbull RB (1997) On Li-bearing micas: estimating Li from electron microprobe analyses and an improved diagram for graphical representation. *Mineralogical Magazine* **61**, 809–34. doi: 10.1180/minmag.1997.061.409.05

Tobisch OT, McNulty BA and Vernon RH (1997) Microgranitoid enclave swarms in granitic plutons, central Sierra Nevada, California. *Lithos* **40**, 321–39. doi: 10.1016/S0024-4937(97)00004-2

Turienzo M, Sánchez N, Lebinson F and Dimieri L (2018) The structure of the Southern Central Andes (Chos Malal Fold and Thrust Belt). In *The Evolution of the Chilean-Argentinean Andes* (eds A Folguera, E Contreras-Reyes, N Heredia, A Encinas, SB Iannelli, V Oliveros, FM Dávila, G Collo, L Giambiagi, A Maksymowicz, MP Iglesia Llanos, M Turienzo, M Naipauer, D Orts, VD Litvak, O Alvarez and C Arriagada), pp. 411–41. Cham: Springer International Publishing. doi: 10.1007/978-3-319-67774-3_17

Vergani GD, Tankard AJ, Belotti HJ and Welsink HJ (1995) Tectonic evolution and paleogeography of the Neuquén Basin, Argentina. In Petroleum Basins of South America (eds AJ Tankard, R Suárez Soruco and HJ Welsink), pp. 383–402. American Association of Petroleum Geologists Memoir no. 62. doi: 10.1306/M62593C19

Vernon RH (1990) Crystallization and hybridism in microgranitoid enclave magmas: microstructural evidence. *Journal of Geophysical Research* **95**, 17849. doi: 10.1029/JB095iB11p17849

Vernon RH (2010) Granites really are magmatic: using microstructural evidence to refute some obstinate hypotheses. *Journal of the Virtual Explorer* **35**, 1–36. doi: 10.3809/jvirtex.2011.00264

Wack MR and Gilder SA (2012) The SushiBar: an automated system for paleomagnetic investigations. *Geochemistry, Geophysics, Geosystems* **13**, 1–24. doi: 10.1029/2011GC003985

Wagner M, Altherr R and Van den haute P (1992) Apatite fission-track analysis of Kenyan basement rocks: constraints on the thermotectonic evolution of the Kenya dome. A reconnaissance study. *Tectonophysics* **204**, 93–110. doi: 10.1016/0040-1951(92)90272-8

Wones DR and Eugster HP (1965) Stability of biotite: experiment, theory, and application. *The American Mineralogist* **50**, 1228–72.

Wyllie PJ, Cox KG and Biggar GM (1962) The habit of apatite in synthetic systems and igneous rocks. *Journal of Petrology* **3**, 238–43. doi: 10.1093/petrology/3.2.238

Yavuz F (2003) Evaluating micas in petrologic and metallogenic aspect: I–definitions and structure of the computer program MICA+. *Computers & Geosciences* **29**, 1203–13. doi: 10.1016/S0098-3004(03)00142-0 AQ27

Zaffarana CB, Somoza R and López de Luchi M (2014) The Late Triassic Central Patagonian Batholith: magma hybridization, $^{40}Ar/^{39}Ar$ ages and thermobarometry. *Journal of South American Earth Sciences* **55**, 94–122. doi: 10.1016/j.jsames.2014.06.006

Zaffarana CB, Somoza R, Orts DL, Mercader R, Boltshauser B, González VR and Puigdomenech C (2017) Internal structure of the Late Triassic Central Patagonian batholith at Gastre, southern Argentina: implications for pluton emplacement and the "Gastre fault system." *Geosphere* **13**, 1973–92. doi: 10.1130/GES01493.1

Žák J, Schulmann K and Hrouda F (2005) Multiple magmatic fabrics in the Sázava pluton (Bohemian Massif, Czech Republic): a result of superposition of wrench-dominated regional transpression on final emplacement. *Journal of Structural Geology* **27**, 805–22. doi: 10.1016/j.jsg.2005.01.012

Zamora Valcarce G (2007) *Estructura y cinemática de la Faja Plegada y Corrida del Agrio, Cuenca Neuquina*. Ph.D. thesis, Universidad de Buenos Aires, Buenos Aires, Argentina. Published thesis.

Zamora Valcarce G, Zapata T and Ramos VA (2011) La Faja Plegada y Corrida del Agrio. In *Relatorio Del XVIII Congreso Geológico Argentino, Neuquén*, pp. 367–74.

Zanettini JCM, Santamaría GR and Leanza H (2001) Hoja Geológica 3772-II, Las Ovejas. Provincia del Neuquén. Buenos Aires: Instituto de Geología y Recursos Minerales, Servicio Geológico Minero Argentino.

Zappettini EO, Chernicoff CJ, Santos JOS, Dalponte M, Belousova E and McNaughton N (2012) Retrowedge-related Carboniferous units and coeval magmatism in the northwestern Neuquén province, Argentina. *International Journal of Earth Sciences* **101**, 2083–104. doi: 10.1007/s00531-012-0774-3

Zappettini EO, Cozzi G, Dalponte M, Godeas M, Korzeniewski LI, Peroni J, Segal S and Castro Godoy S (2021) Análisis Geológico y Metalogenético del Sector Norte de la Cordillera del Viento, Provincia del Neuquén. Buenos Aires: Instituto de Geología y Recursos Minerales, Servicio Geológico Minero Argentino. Serie Contribuciones Técnicas Recursos Minerales no. 44, 51 pp.

Zappettini E, Korzeniewski LI and Segal S (2014) Nuevos datos de las mineralizaciones polimetálicas del distrito Varvarco, Neuquén. In *19º Congreso Geológico Argentino, Córdoba*. p. S6-4.

Zappettini EO, Lagorio SL, Dalponte M, Orestes J and Belousova E (2018) Evidencias de magmatismo precuyano (Pliensbachiano – Toarciano) en el norte de la Cordillera del Viento, provincia del Neuquén: caracterización geoquímica, isotópica e implicancias tectónicas. *Revista de la Asociación Geológica Argentina* **75**, 533–58.

Zappettini E, Méndez V and Zanettini JC (1987) Metasedimentitas mesopaleozoicas en el noroeste de la Provincia del Neuquén. *Revista de la Asociación Geológica Argentina* **42**, 206–7.